



GAUDÍ, THE FORMS THAT EXPRESS GENIUS

Author: Norberto Mangiavacchi¹ norberto@uerj.br

¹ State University of Rio de Janeiro

January 21, 2015

PPG-EM Seminars: season 2015
www.ppg-em.uerj.br

Keywords: Natural forms, Nature, physical phenomena, geometric, mathematical principles, architecture.

1 Introduction

As researchers dedicated to understand and explain physical phenomena, we frequently encounter geometric forms that are particularly appealing to our senses and intellects. Hydrodynamic instabilities, buckling of structures, pattern formation in many physical systems, two-phase flows with moving interfaces, waves, to name a few, produce interesting shapes for their aesthetic impression and for their physical properties. Looking at Spanish Catalan architect Antoni Gaudí i Cornet artistic creations we recognize, as in a déjà vu, some of the same geometric forms. Gaudí's works reflect an individualized and distinctive style. Under the influence of neo-Gothic art and Oriental techniques, Gaudí became part of the Modernista movement which was reaching its peak in the late 19th and early 20th centuries. His work transcended mainstream Modernisme, culminating in an organic style inspired by natural forms. The forms created and employed by Gaudí in his architectural creations are inspired by an acute observation of the nature. "Everything comes from the Great Book of Nature" he had said.

The works of Gaudí materialize from geometric elements that have much in common with those found in the investigation of problems faced by researchers in applied science. Examples range from simple forms like the catenary curve and catenoid (arising by rotating a catenary curve about its directrix), to complex patterns and fractals common in dynamic systems. We know how similar differential equations seem to appear recurrently in problems very different from the physical perspective and very similar from the mathematical point of view, giving origin to patterns, shapes and behaviors, in space and time, that are conspicuous. Anthropomorphic, animal and vegetal shapes, as bones, shells, leaves, are derived from solutions of problems based in physical laws. These entities exist in the universe since its origin, following nature and human development, thus impregnating our collective unconscious and making part and dictating the behavior of our own physical stuff. It is not surprising that humans have an emotional response to natural elements. Examples of Gaudí thoughts and architectural creations, that illustrate his acute observa-

tion of nature, and the genial combination of a positive aesthetic and emotional response with very effective technical solutions in every detail, will be presented. In these examples we will point to some connections of the geometric forms with physical phenomena and their mathematical description.

2 Light

Architecture is the arrangement of light; sculpture is the play on light.

"Light achieves maximum harmony at an inclination of 45 degrees, since it resides on objects in a way that is neither horizontal nor vertical. This can be considered medium light, and it offers the most perfect vision of objects and their most exquisite nuances. It is the Mediterranean light. Paraboloids, hyperboloids and helicoids, constantly varying the incidence of the light, are rich in nuances themselves, which make ornamentation and even modeling unnecessary"

3 Waves, linear and non-linear, free-surfaces and interfaces, dynamic systems, patterns and fractals

"Form does not necessarily follow function."

"Nothing is invented, for it's written in nature first. Anything created by human beings is already in the great book of nature."

"Everything comes from the great book of nature."

"Originality implies a return to the origins, original is returning to the simplicity of the first solutions."

"The creation continues incessantly through the media of man. But man does not create... he discovers."

4 Conclusion

"Men may be divided into two types: men of words and men of action. The first speaks; the latter act. I am of the second group. I lack the means to express myself adequately. I would not be able to explain to anyone my artistic concepts. I have not yet concretized them. I never had time to reflect on them. My hours have been spent in my work."

Not all artists are so inspired by nature as Gaudí. We, as scientist, can draw inspiration in Gaudí's example.



Figure 1: Left and center: La Sagrada Família. Shades of light and geometrical forms: The catenary, the catenoid, ruled surfaces and fractals. Right: Casa Batlló. Helicoids and catenaries. Gaudí took care of every detail of all structural and ornamental elements, always making sure that his constructions had good lighting and ventilation. His study of nature translated into his use of ruled geometrical forms such as the hyperbolic paraboloid, the hyperboloid, the helicoid and the cone. Gaudí found abundant examples of ruled surfaces in nature, for instance in plants, shells and bones. These forms are at the same time functional and aesthetic, and Gaudí discovered how to adapt the language of nature to the structural forms of architecture.



Figure 2: Top: The roof of La Pedrera, showing wavy shapes, some typical of buckling. Left: Interior of Casa Batlló, showing surfaces found hydrodynamics, and employing adaptive tessellation of complex surfaces. Right: Roof of Casa Batlló: textures, that enhance the perception of forms, are found in many nonlinear dynamic systems, like in pattern formation and nonlinear surface waves.

References

- [1] Antoni gaudí. https://en.wikipedia.org/wiki/Antoni_Gaud%C3%AD. Accessed: 2015-01-10.
- [2] C. Browne. Gaudí's organic geometry. *Chaos and Graphics*, I:105–115, 2008.
- [3] J.E. Cirlot. *Gaudí, Introduzione alla sua Architettura*. Triangle Postals – España, 2007.
- [4] M.G. Lorenzi and M. Francaviglia. Art & mathematics in antoni gaudi's architecture: "la sagrada familia". *Journal of Applied Mathematics*, III:0–10, 2010.



LINEAR STABILITY ANALYSIS OF FINGERING IN CONVECTIVE DISSOLUTION IN POROUS MEDIA

Rachel Lucena

Supervisors: Prof. PhD Norberto Mangiavacchi ¹
 Prof. PhD José Pontes ¹

¹ State University of Rio de Janeiro, Mechanical Engineering Department

1 Introduction

Fingering refers to hydrodynamic instabilities of deforming interfaces into fingers during the displacement of fluids in porous media. These instabilities are closely linked to changes in viscosity or density between the different layers or within a single phase containing a solute invariable concentration that affects the fluid density or viscosity (Homsy [3]). The phenomena occurs in a variety of applications, including CO₂ sequestration techniques, secondary and tertiary crude oil recovery, fixed bed regeneration chemical processing, hydrology, filtration, liquid chromatography, and medical applications, among others. In fact, the phenomena are expected to occur in different fields of science and technology, in which flows in porous media are present.

We consider the problem of buoyancy-driven fingering generated in porous media by the dissolution of a fluid layer initially placed over a less dense one in which it is partially miscible. The focus is on the lower layer only where the convective dissolution dynamics takes place.

A 2D time dependent numerical simulation is performed, assuming that the flow is governed by Darcy's law, along with the Boussinesq approximation to account for buoyancy effects introduced by a concentration dependent density. The viscosity is assumed as constant. A vorticity-stream function formulation is adopted to solve the hydrodynamic field (Almarcha et al. [1], Budroni et al. [2]).

1.1 Model equations

The equations describing the dynamics in the flow field that governing the evolution of the concentration field are:

$$\nabla^2 \psi = -\omega_z \quad (1)$$

$$\omega_z = R \frac{\partial c}{\partial x} \quad (2)$$

$$\frac{Dc}{Dt} = \mathcal{D} \nabla^2 c, \quad (3)$$

where: ψ is the stream function ($\mathbf{u} = (\partial\psi/\partial y, -\partial\psi/\partial x)$), ω_z is the vorticity ($\omega_z = \nabla^2 \psi$), $R = -\beta g i_z$, c is the concentration field and \mathcal{D} is the diffusion coefficient. Equation 1 is the vorticity equation, Eq. 2 is Darcy's Law for the vorticity and Eq. 3 is the concentration transport equation.

2 Linear Stability Analysis (LSA) of the Base State

The base state of the problem is the time dependent solution of Eq. 3 of the concentration field in absence of any flow:

$$\bar{c}(y, t) = 1 - \text{erf}\left(\frac{y}{2\sqrt{t}}\right). \quad (4)$$

On the basis of Eqs. 1-3, a LSA can be performed to obtain dispersion curves giving the growth rate of the perturbations as a function of the wavenumber.

The LSA consists in adding perturbations to the base state solution characterized by the concentration profile (4) and

$$\begin{pmatrix} c \\ \psi \end{pmatrix} = \begin{pmatrix} \bar{c} \\ 0 \end{pmatrix}(y, t) + \begin{pmatrix} \tilde{c} \\ i\tilde{\psi} \end{pmatrix}(y) \exp(\sigma t + ikx), \quad (5)$$

where $i^2 = -1$, k is the wavenumber of the perturbation and σ is the growth rate. The linearised evolution equations for the disturbances \tilde{c} and $\tilde{\psi}$ are thus:

$$\tilde{\psi}_{yy} - k^2 \tilde{\psi} = k^2 \tilde{c} \quad (6)$$

$$\sigma \tilde{c} + \tilde{\psi} \tilde{c}_y = \tilde{c}_{yy} - k^2 \tilde{c} \quad (7)$$

Boundary conditions for the concentration and stream function perturbations \tilde{c} and $\tilde{\psi}$ are thus:

$$y = 0 : \quad \tilde{c} = 0, \quad \tilde{\psi} = 0$$

$$y \rightarrow \infty : \quad \tilde{c} \rightarrow 0, \quad \tilde{\psi} \rightarrow 0.$$

Upon defining $D^n = d^n/dy^n$, we rewrite Eq. 6: $(D^2 - k^2) \tilde{\psi} = k^2 \tilde{c}$ and inversely: $\tilde{\psi} = (D^2 - k^2)^{-1} k^2 \tilde{c}$.

Upon replacing $\tilde{\psi}$ in Eq. 7 and rearranging terms we arrive

at an eigenvalue-eigenfunction equation for the rate of growth σ and associated vertical concentration profile in the form:

$$\left[(D^2 - k^2) - (D^2 - k^2)^{-1} k^2 D \bar{c} \right] \tilde{c} = \sigma \tilde{c}.$$

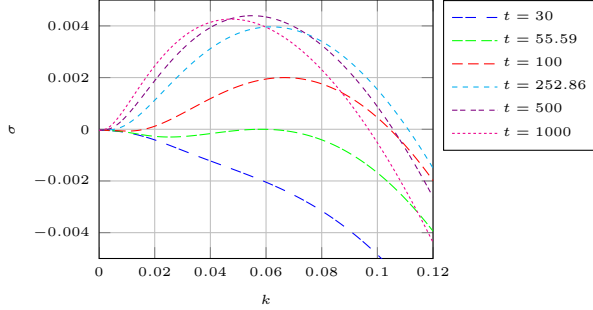


Figure 1: Dispersion curves.

Figure 1 shows the dispersion curves of normal mode perturbations of the base state, numerically obtained for several times. All perturbations are damped for $t < 55.59$. A bifurcation occurs at $t = 55.59$ when the first perturbation becomes marginally stable with a wavenumber $k = 0.06192$.

2.1 Deployment of instabilities with variable and frozen base state

This section reports the experiments conducted to evaluate the rate of growth of modes with the wavelength λ associated to $k_0 = 0.06192$. We denote this mode as “mode 4”. Initial condition used in the experiments consisted of the base state at $t = 252$ plus perturbation with this wavenumber.

We investigate the deployment of instabilities with a time dependent base state by numerically integrating Eqs. 1-3.

We also investigate the rate of growth of perturbations with frozen base state. In order to extract the amplitude of mode 4 we adopted the following procedure:

1. The base state is subtracted from result of the numerical result of integration, both at the same time;
2. The result is integrated along the y direction, followed by evaluation of the Fourier transform of the result, giving the sought amplitude.

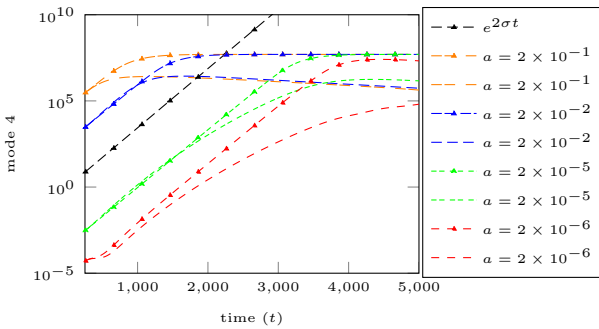


Figure 2: A comparison between the evolution of the amplitude of mode 4 with frozen base state (curves with marks) and evolving base state (curves without marks) for initial amplitudes as given in the figure.

Fig. 3 presents a plot of the rate of growth σ as a function of time with frozen base state (curves with marks) and evolving base state. This figure confirms that the rate of growth obtained from the numerical integration of the evolution equations matches the “exact” value from the linear stability analysis during the stages of linear growth.

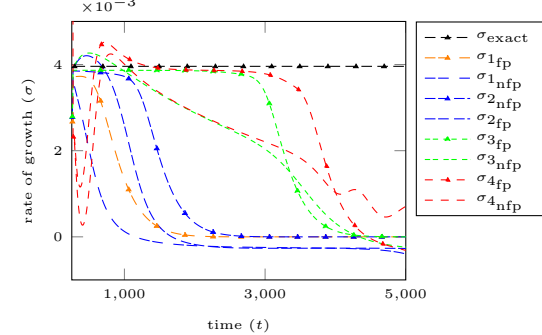


Figure 3: A comparison between the evolution of the rate of growth of mode 4 with frozen base state (curves with marks) and evolving base state (curves without marks) with the different initial amplitudes a of the perturbation (mode 4). $\sigma_{1\text{fp}}$ and $\sigma_{1\text{nfp}}$ refer to amplitude $a = 2 \times 10^{-1}$, $\sigma_{2\text{fp}}$ and $\sigma_{2\text{nfp}}$ to amplitude $a = 2 \times 10^{-2}$, $\sigma_{3\text{fp}}$ and $\sigma_{3\text{nfp}}$ to amplitude $a = 2 \times 10^{-5}$, $\sigma_{4\text{fp}}$ and $\sigma_{4\text{nfp}}$ to amplitude $a = 2 \times 10^{-6}$.

3 Conclusions

We observed that when integrating the evolution equation starting from the base state plus a perturbation a minimum initial level of this one is required to obtain the linear growth of the linear stability analysis in the first stages of evolution. If this minimum is not included in the initial condition a deviation occurs at the first stages of the linear growth, due to noise introduced by the grid.

As we allow the base state to evolve we observe a certain deviation in the rate of growth of the amplitude of modes when comparing with σ obtained from the linear analysis, due to nonlinear effects.

We conclude then that the increase in the interface gradient enhances dissolution of CO_2 .

References

- [1] C. Almarcha, P.M.J. Trevelyan, P. Grosfils, and A. De Wit. Chemically driven hydrodynamics instabilities. *Physical Review Letters*, 104:044501–(1–4), 2010.
- [2] M.A. Budroni, L.A. Riofio, L. Lemaigre, F. Rossi, M. Rustuci, and A. De Wit. Chemical control of hydrodynamics instabilities in partially miscible two-layer systems. *Journal of Physical Chemistry Letters*, 5:875–881, 2014.
- [3] G.M. Homsy. Viscous fingering in porous media. *Annu. Rev. Fluid Mechanics*, 19:271–311, 1987.

PASSIVE COOLING SYSTEMS

Leon Lima

Supervisor: Prof. PhD Norberto Mangiavacchi

February 22, 2015

1 Introduction

Passive Cooling Systems (PCS') are engineering solutions to perform the function of heat transfer using the temperature difference between hot and cold sources to generate the driving force. They are, therefore, autonomous systems, independent of external energy sources. Most of the designs consists of heat exchangers connected by a hydraulic circuit. Because they don't need active components to operate, PCS' have the advantages of lower costs and higher reliability. Nowadays, PCS' find large applicability in

cooling functions of electronic components and in the nuclear industry. Indeed, the high reliability make these systems particularly relevant to nuclear installations, especially after the events of Fukushima¹

PCS' can be classified as single-phase and two-phase systems. There is a third class which operate at very high temperatures and pressures: the supercritical systems, which are single-phase with characteristics of two-phase systems. Many fossil fuel fired power plants use supercritical water because of the high efficiency of the thermal cycle. While conventional cycles

¹Nuclear accident caused by a strong seismic event succeeded by a tsunami in the east coast of Japan.

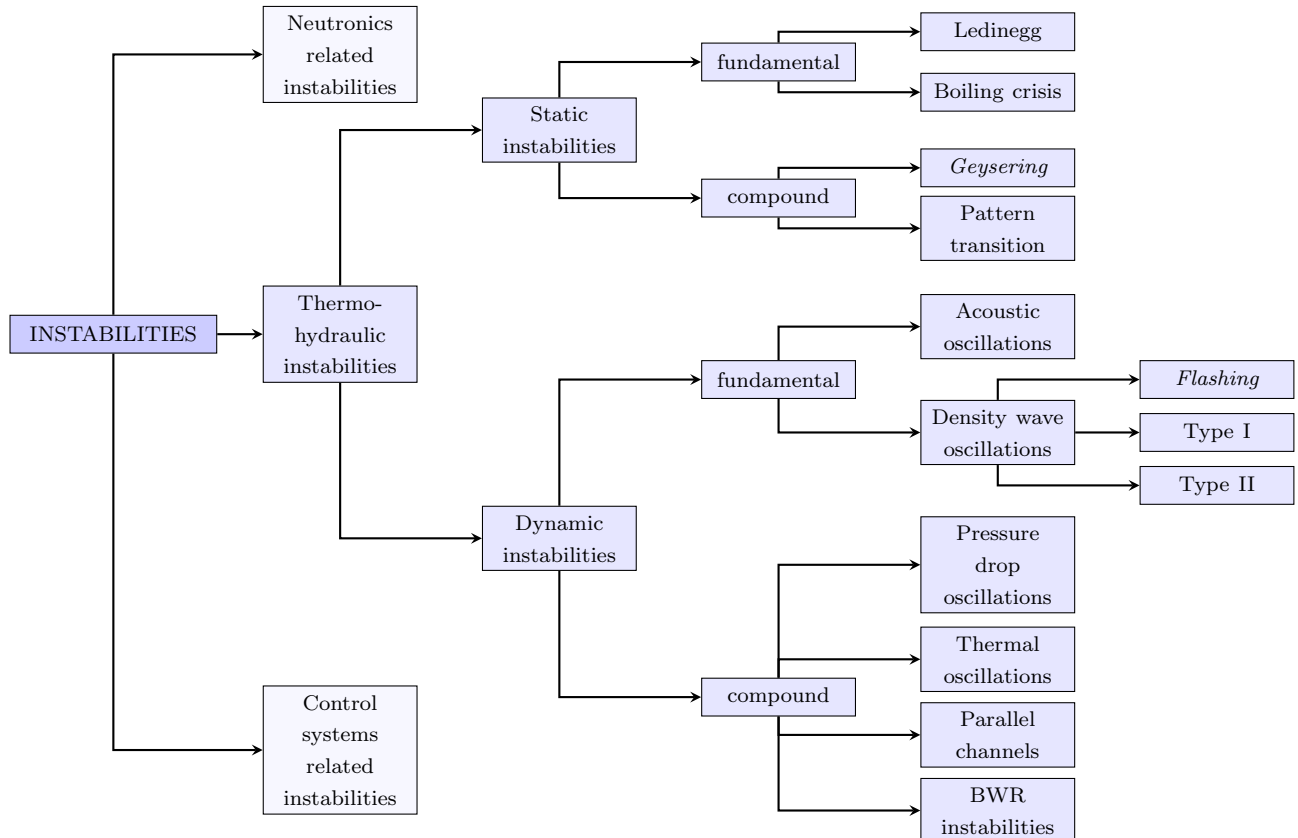


Figure 1: Instability types according to Prasad et al. [3].

may have efficiencies up to 36%, supercritical cycles may provide up to 50% efficiency [4]. Additionally, the design of passive systems with supercritical fluids is favored by the high density gradients close to pseudo-critical points². One of the design of Generation IV nuclear reactors³ consists of a reactor cooled by supercritical water, possibly in a passive system.

Nevertheless, independent of the type, all PCS' have the disadvantage of being subjected to instabilities, which may lead to inadmissible levels of vibrations and generate high temperature spots in the circuit. Although two-phase systems are much more susceptible to instabilities, there are conditions in which single-phase systems can be unstable.

2 Stability in a PCS

The interplay between buoyancy forces and friction drag after a perturbation may generate increasing oscillations in the system's transient properties. In this case, the PCS is unstable and the instability is a dynamic type one. In fact, instabilities of cooling circuits can be of many different types. Boure et al. [1] is one of the first works to provide a classification of instabilities in two-phase systems (including active systems) and is the basis for the classification used today by many authors for natural circulation loops, both single and two-phase. Their work presents 10 types of instabilities, divided into two main classes: static and dynamic instabilities. Prasad et al. [3] identified the types studied by Boure et al. [1] as thermo-hydraulic instabilities, and added two other groups aside this: the instabilities associated to control systems and the ones associated to neutron kinetics (see fig. 1).

2.1 Stability in a single-phase PCS

In a work published on 1975, Creveling et al. [2] estimate that, in previous works, instabilities in single-phase natural circulation loops were only reported for systems operating at conditions close to the pseudo-critical point. They mention, however, analytical results published between 1966 and 1967 which concluded that there are conditions under which subcritical single-phase systems present instabilities. Motivated by this evidence, Creveling et al. [2] were the

first work to show experimental results with unstable behavior in a conventional (subcritical) single-phase natural circulation loop. Today there is a wide knowledge about instabilities in single-phase systems. For example, Vijayan et al. [5] estate that stability in such systems depend on the

- Grashof and Stanton numbers⁴;
- flow regime;
- heater and cooler orientation;
- length scales of the loop (height, total length, heater and cooler lengths etc.).

There are many experimental and numerical results available today which reproduce instabilities, both static and dynamic, in several geometries of conventional single-phase natural circulation loops. Natural convection flows without phase change in closed circuits occur in many types of nuclear installations, like in most of pressurized reactors in case of loss of reactor coolant pumps, and it is also the type of flow during start up of boiling water reactors.

References

- [1] J. A. Boure, A. E. Bergles, and L. S. Tong. Review of two-phase flow instability. *Nuclear Engineering and Design*, 25:165–192, 1973.
- [2] H.F. Creveling, J.F. De Paz, J.Y. Baladi, and R.J. Schoenhals. Stability characteristics of a single-phase free convection loop. *Journal of Fluid Mechanics*, 67:65–84, 1975.
- [3] Gonella V. Durga Prasad, Manmohan Pandey, and Manjeet S. Kalra. Review of research on flow instabilities in natural circulation boiling systems. *Progress in Nuclear Energy*, 49:429–451, 2007.
- [4] T. Schulenberg, L. K. H. Leung, and Yoshiaki Oka. Review of R&D for supercritical water cooled reactor. *Progress in Nuclear Energy (article in press)*, 2014.
- [5] P.K. Vijayan, M. Sharma, and D. Saha. Steady state and stability characteristics of single-phase natural circulation in a rectangular loop with different heater and cooler orientations. *Experimental Thermal and Fluid Sciences*, 31:925–945, 2007.

²For each isobaric curve above the thermodynamic critical pressure, there is a supercritical temperature which defines a pseudo-critical point in this isobaric at which the specific heat at constant pressure exhibits a maximum value.

³www.gen-4.org

⁴These non-dimensional numbers are presented in a modified form by Vijayan et al. [5]



PARTICLE TRANSPORT MODELING IN CHANNEL STEADY LAMINAR AND TURBULENT

Author: Apoena Calil and Gabriel Meletti¹

¹ State University of Rio de Janeiro

apoenacalil@gmail.com, gabrielmeletti@gmail.com

June 22, 2015

PPG-EM Seminars: season 2015
www.ppg-em.uerj.br

1 Introduction

In this work, the physical processes responsible for the transport of particles in regular channels for turbulent flow regimes are modeled. Particle transport is a relevant area of knowledge with many applications, such as the transport of sand or paraffin in pipelines and blood flow. To account for the turbulent effects, the “zero-equation” RANS model was employed, which makes use of the concept of turbulent viscosity proposed by Boussinesq. Effects along the vertical direction (channel’s depth) was neglected and the flow was considered completely developed, allowing for a 1D approach.

Particle transport was described by the BBO equation [1], through a Lagrangian approach, considering drag, lift, virtual mass and gravity as the forces which act on the particles.

The flow followed a Eulerian approach, using centered finite differences for space domain discretization and both explicit and implicit formulations were implemented. One-way coupling between flow and particles was considered, meaning that only the flow affected the particles, with no feedback from particles to the flow.

Results for the flow profile showed good results and, although preliminary, results for the particle transport showed physical coherence, in accordance to the applied forces.

2 Flow modeling

Taking into account that the flow is developed and incompressible, the RANS equations that describe the flow, already incorporating the concept of Boussinesq viscosity, is given by

momentum:

$$\frac{\partial u}{\partial t} = -\frac{1}{\rho} \frac{\partial p}{\partial x} + \frac{\partial}{\partial y} \left[(\nu_m + \nu_t) \frac{\partial u}{\partial y} \right] \quad (1)$$

continuity:

$$\frac{\partial u}{\partial x} = 0 \quad (2)$$

where u is the longitudinal velocity component, t is time, ρ is the density of the fluid, p is pressure, x and y are the longitudinal and orthogonal coordinates of the channel domain, ν_m is the kinematic viscosity of the fluid,

designated as “molecular viscosity” in opposition to the turbulent, or apparent, viscosity, which results from the turbulence. Note that u and p actually represent the mean values of velocity and pressure fields.

The Prandtl mixing length model (algebraic model) was used for characterization of the turbulent viscosity, which means that

$$\nu_t = l_c^2 \left| \frac{\partial u}{\partial y} \right| \quad (3)$$

where l_c is the mixing length, defined as

$$l_c = \kappa y, \text{ para } y \leq \delta \quad (4a)$$

$$l_c = \kappa \delta, \text{ para } y > \delta \quad (4b)$$

with κ as Von Kármán’s constant and δ as the boundary layer thickness. Motion equations are solved using Centered Finite Differences for space discretization, making use of a staggered grid.

3 Particles

From the point of view of the model, particles are transported through a Lagrangian approach, so that an Eulerian-Lagrangian formulation characterizes the fluid-particles modeling. One-way coupling between flow and particles was considered, which means that particles do not make influence on the flow. The transport is modelled by a form of the BBO equation, taking into account four forces: drag, lift, virtual mass and gravity. For more details concerning the BBO equation, please refer to [1], section 4.3. The influence of the turbulent regime on the particles is simulated by means of the so-called discrete eddy model, which applies a random perturbation into the velocity components of the particles based on the magnitude of the turbulent viscosity.

The four forces taken into account in the model are expressed by the following equations:

drag force \mathbf{F}_D :

$$\mathbf{F}_D = 3\pi\mu D(\mathbf{u} - \mathbf{v}_p) \quad (5)$$

lift force \mathbf{F}_L :

$$\mathbf{F}_L = 1.61\sqrt{\mu\rho_p}D^2 \parallel \mathbf{u} - \mathbf{v}_p \parallel \frac{d\mathbf{u}}{dy} \left| \frac{du}{dy} \right|^{-0.5} \quad (6)$$

added mass force \mathbf{F}_{AM} :

$$\mathbf{F}_{AM} = \frac{1}{2} M \frac{d\mathbf{v}_p}{dt} \quad (7)$$

gravity force \mathbf{F}_G :

$$\mathbf{F}_G = Mg \quad (8)$$

where ρ_p , D and \mathbf{v}_p are respectively the particle's density, diameter and velocity vector; \mathbf{u} is velocity vector of the flow. Both \mathbf{u} and \mathbf{v}_p have two components in the present model.

The trajectory of the particles are computed by solving

$$\Sigma \mathbf{F} = \mathbf{F}_D + \mathbf{F}_L + \mathbf{F}_{AM} + \mathbf{F}_G = M \frac{d\mathbf{v}_p}{dt} \quad (9)$$

which is a form of the BBO equation. An additional perturbation \mathbf{v}'_p is applied on the particles' velocity due to turbulence contributions. The perturbation is defined by the discrete eddy model, using Gaussian distribution to account for the random characteristic, i.e.

$$\mathbf{v}'_p = 4\zeta l_c \sqrt{2/3} \left| \frac{\partial u}{\partial y} \right| \quad (10)$$

The factor ζ is computed by a Monte Carlo like iterative procedure, in which two random values ζ and f_R are generated, with $\zeta \in [-0.5, 0.5]$ and $f_R \in [0, 1/\sqrt{2\pi}]$. If $f_R \leq f$, where $f = 1/\sqrt{2\pi} \exp(-0.5\zeta^2)$ (Gaussian function), then ζ is the factor used to compute the velocity fluctuation. Otherwise, a new pair of random values ζ and f_R is generated, and the procedure is repeated until the condition $f_R \leq f$ is satisfied. Equation 9 is a linear ODE that can be analytically solved for \mathbf{v}_p . Thus, the new position \mathbf{x}^{n+1} of each particle in the time step $n+1$ is computed in a Lagrangian way using the turbulent particle velocity $\mathbf{v}_p + \mathbf{v}'_p$, i.e.,

$$\mathbf{x}_p^{n+1} = \mathbf{x}_p^n + (\mathbf{v}_p + \mathbf{v}'_p) \Delta t \quad (11)$$

where Δt is the time increment.

4 Results

Three results will be presented: two velocity profiles, one for steady laminar and another for steady turbulent regime, and a frame from one simulation of particles transport. Laminar profile is obtained from solving eq.1 with $\partial u / \partial t = 0$ and $\nu_t = 0$. The numerical results were compared to analytical solution. Figure 1 shows the comparison for $Re = 10^3$ with a mesh of 80 nodes.

In fig. 2, the non-dimensional turbulent boundary layer is shown, for $Re = 10^5$ and a mesh of 800 nodes. Comparison is qualitative good.

Now, 20 particles were randomly distributed in the channel, with null initial velocity, in a turbulent flow regime. Figure 3 shows a frame of the simulation.

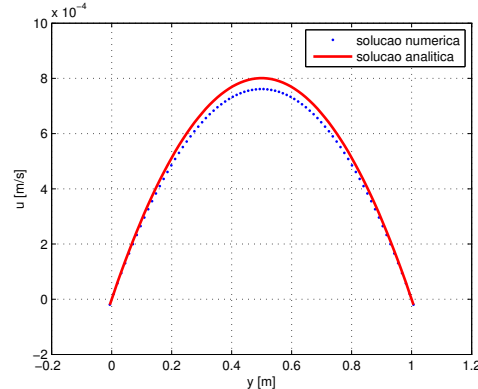


Figure 1: Numerical and analytical laminar profiles of channel flow with $Re = 10^3$.

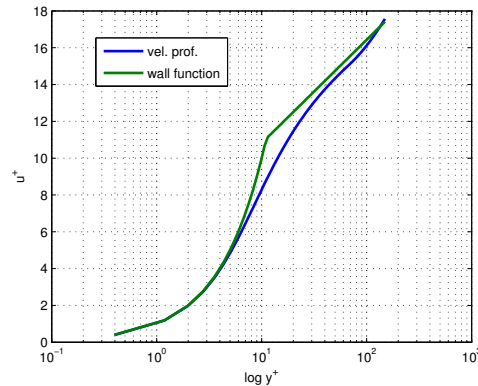


Figure 2: Comparison of turbulent channel flow result with wall function, for $Re = 10^5$.

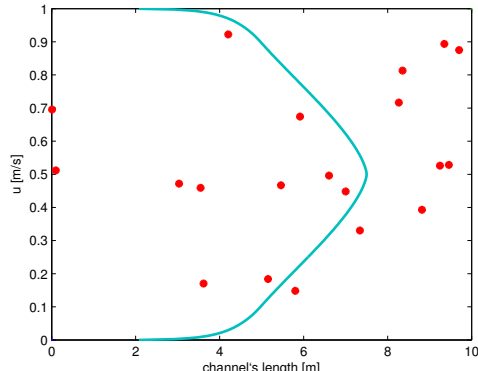


Figure 3: Particles transported by turbulent flow in the channel.

5 Conclusion

The numerical model implemented provides accurate results for the velocity profiles, but results for particle transport still need to be validated. However, the model covers several areas of CFD, such as basic turbulence modeling, finite difference method, numerical diffusion, particle transport, and serves as a complete learning tool.

References

- [1] Clayton T. Crowe, John D. Schwarzfeld, Martin Sommerfeld, and Yutaka Tsuji. *Multiphase flows with droplets and particles*. CRC Press, 2012.



NANO-PATTERNING OF SURFACES BY ION SPUTTERING: NUMERICAL STUDY OF AN ANISOTROPIC KURAMOTO-SIVASHINSKY EQUATION

Author: Vitral, E.¹ eduardo.vitral@gmail.com
Advisor(s): Gustavo Rabello dos Anjos¹; José da Rocha Miranda Pontes¹

¹ State University of Rio de Janeiro

May 7, 2015

PPG-EM Internal Seminars: Season 2015
www.ppg-em.uerj.br

Keywords: Kuramoto-Sivashinsky equation, sputtering, finite-difference method.

1 Introduction

Ion beam sputtering is one important technology which operates in nonequilibrium conditions and allows the processing of materials and structures outside the limits of the equilibrium thermo-dynamics. The theoretical comprehension of such process is still an ongoing challenge and their mathematical modeling needs more development. Our effort aims toward the implementation of a numerical scheme to solve a model proposed to the ion beam sputtering erosion.

The phenomenon consists on the ionic bombardment of a surface, spontaneously developing a well-ordered periodicity over a large area under certain conditions. This physical process responsible for the formation of periodic structures on the previously surface is called sputtering. Depending on the energy of the incident ion, a train of collision event may be established, resulting in the ejection of atoms from the matrix. The morphology of the surface can drastically change due to these sputtered atoms, being responsible for the appearance of unexpectedly organized patterns, such as ripples and hexagonal arrays of nanoholes.

The Kuramoto-Sivashinsky equation is deterministic and highly nonlinear, being capable of producing a great variety of morphologies, making it a strong candidate to represent the complex structure formation on sputtered surfaces. In the present endeavor, a finite-difference semi-implicit splitting scheme of second order in time and space is proposed to numerically solve an anisotropic Kuramoto-Sivashinsky equation subjected to periodical boundary conditions for two dimensional surfaces.

2 Numerical scheme

One of the simplified and dimensionless form of the anisotropic Kuramoto-Sivashinsky reads:

$$\begin{aligned} \frac{\partial \bar{h}}{\partial \tau} = & -\bar{\alpha} \bar{h} + \bar{\mu} \frac{\partial^2 \bar{h}}{\partial X^2} - c^2 \frac{\partial^2 \bar{h}}{\partial Y^2} + \bar{\nu}_x \left(\frac{\partial \bar{h}}{\partial X} \right)^2 - c^3 \left(\frac{\partial \bar{h}}{\partial Y} \right)^2 \\ & - D_{XX} \frac{\partial^4 \bar{h}}{\partial X^4} + D_{XY} \frac{\partial^4 \bar{h}}{\partial X^2 \partial Y^2} + c^2 \frac{\partial^4 \bar{h}}{\partial Y^4} \\ & - \bar{K} \left(\frac{\partial^4 \bar{h}}{\partial X^4} + 2 \frac{\partial^4 \bar{h}}{\partial X^2 Y^2} + \frac{\partial^4 \bar{h}}{\partial Y^4} \right) \end{aligned} \quad (1)$$

where \bar{h} and τ are, respectively, the surface height function of the external atom layer and the time dependency of the transient model, with X and Y as the domain space coordinates. The function c represents the cosine of the incident angle θ . Equation 1 presents a damping term $-\bar{\alpha} \bar{h}$, with α being damping coefficient, contributing to the smoothening of the surface. Finally, K takes into account the surface diffusion effects, which varies with temperature. The parameters μ , ν_x , D_{XX} and D_{XY} are anisotropy coefficients and also function of θ .

We propose the following second order in time Crank-Nicolson semi-implicit scheme for solving Equation 1 with $a_\mu = 4$, high temperatures and $< 65.3^\circ$ [1]:

$$\frac{\bar{h}^{n+1} - \bar{h}^n}{\Delta \tau} = \Lambda_X \frac{\bar{h}^{n+1} + \bar{h}^n}{2} + \Lambda_Y \frac{\bar{h}^{n+1} + \bar{h}^n}{2} + f^{n+1/2}$$

Since the operators $\Lambda_X^{n+1/2}$, $\Lambda_Y^{n+1/2}$ and the function $f^{n+1/2}$ contain terms in the new stage we do internal iterations at each time step according to:

$$\begin{aligned} \frac{\bar{h}^{n,m+1} - \bar{h}^n}{\Delta \tau} = & \Lambda_X (\bar{h}^{n,m+1} + \bar{h}^n) \\ & + \Lambda_Y (\bar{h}^{n,m+1} + \bar{h}^n) + f^{n+1/2} \end{aligned}$$

The splitting is made according to the Douglas second scheme [2]

$$\begin{aligned} \frac{\tilde{\bar{h}} - \bar{h}^n}{\Delta \tau} = & \Lambda_X \tilde{\bar{h}} + \Lambda_Y \bar{h}^n + f^{n+1/2} + (\Lambda_X + \Lambda_Y) \bar{h}^n \\ \frac{\bar{h}^{n,m+1} - \tilde{\bar{h}}}{\Delta \tau} = & \Lambda_Y (\bar{h}^{n,m+1} - \bar{h}^n) \end{aligned}$$

3 Results and Discussion

3.1 Initial Pattern: Random Structure

The first case analyzed was for a mesh with 256×256 points with a randomly generated initial pattern, ranging from 0 to 0.1. Since the linear stability analysis reveals a value of $\lambda_c = 18$ for the critical wavelength corresponding to the maximum growth rate in the \vec{I}_x direction, each wavelength of the final pattern was expected to be represented by approximately 9 points.

Figure 1 shows the steady state hexagonal structure clear of defects, after the emergence of hexagonal modes from the initial random pattern. The Fast Fourier Transform (FFT) is also displayed for the central part of the domain (Figure 2).

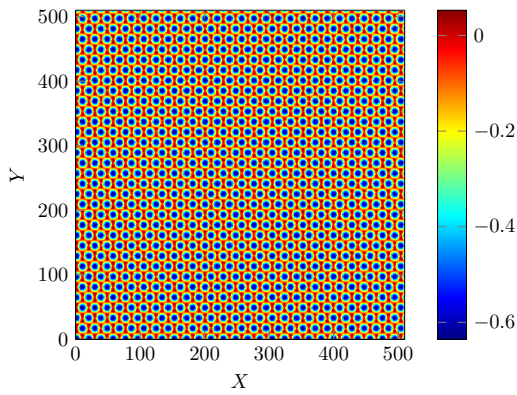


Figure 1: \bar{h}_n Top XY view for $\tau = 49,200$

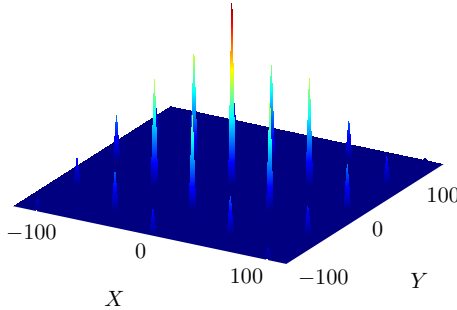


Figure 2: \bar{h}_n Fourier Transform for $\tau = 49,200$

3.2 Initial Pattern: Monomode $\vec{q} = q_o \vec{I}_x$

Another case of interest studied was for an initial pattern with sine function in the X direction, which represents a monomode 1D structure with wavevector $\vec{q} = q_o \vec{I}_x$. The pattern started with 14 wavelengths, being approximately half of the total number of wavelengths in the steady state from the previous case, which agrees with the critical wavelength calculated from the linear stability analysis and is placed inside the stable domain. Figure 3 displays the final state obtained, which is a 1D structure with 27 wavelengths, and Figure 4 shows its Fourier Transform. The wave amplitude goes initially from $(0;0.1)$ to $(-0.4;0)$ in the final state, which is also consistent with the physical phenomenon of surface erosion. Although it seems that the steady

state was reached, hexagonal modes are expected to grow after more time steps.

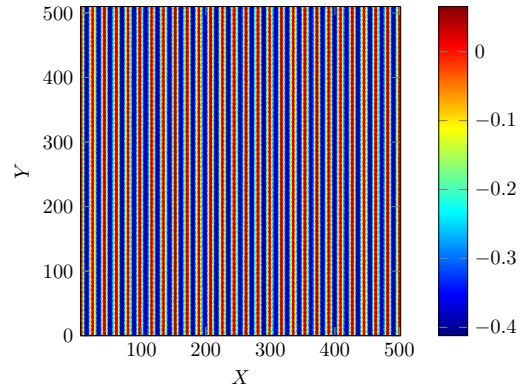


Figure 3: \bar{h}_n Top XY view for $\tau = 150$

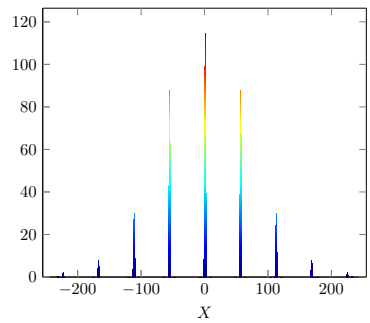


Figure 4: \bar{h}_n Fourier Transform for $\tau = 150$

4 Conclusions

In the present paper we have developed a finite-difference time splitting scheme for solving an anisotropic Kuramoto-Sivashinsky equation to describe a surface eroded by ion bombardment. Hexagonal patterns grew from a domain with random initial conditions, and for the monomode $\vec{q} = q_o \vec{I}_x$ case the wavelength split in two, meeting the critical wavenumber from the linear stability analysis. Both simulations were physically consistent with the sputtering phenomenon, reproducing ripple and hexagonal structure formation dynamics.

5 Acknowledgments

Eduardo Vitral acknowledges a fellowship from CAPES. A FAPERJ Senior Researcher Fellowship is acknowledged by José Pontes.

References

- [1] CI Christov, J Pontes, Daniel Walgraef, and Manuel García Velarde. Implicit time splitting for fourth-order parabolic equations. *Computer methods in applied mechanics and engineering*, 148(3):209–224, 1997.
- [2] Nicolay Nicolayevich Yanenko. *The method of fractional steps*. Springer, 1971.

STABILIZED HYBRIDIZED FINITE ELEMENT FORMULATIONS: A NEW APPROACH

Cristiane Oliveira de Faria¹

¹ Rio de Janeiro State University, IME, Mathematical Analysis Department

1 Introduction

In linear elasticity problems by using of usual displacement-based finite element methods, we are able to numerically determine the displacement field directly and the stresses are evaluated by post-processing. It is well known that standard Galerkin finite element approximations degrade when the Poisson's ratio tends to 1/2, corresponding to near incompressible elasticity.

Hybrid methods are characterized by weakly imposing continuity on each edge of the elements through the Lagrange multipliers. In contrast to DG methods, hybrid formulation allows an element-wise assembly process and the elimination of most degrees of freedom at the element level resulting a global system involving only the degrees-of-freedom of the Lagrange multiplier.

Based on hybridization techniques Faria et al [1, 2] propose a primal hybrid finite element method for the displacement field combining the advantages of DG methods with an element based data structure and reduced computational cost. As multiplier was chosen the trace of displacement field. Stabilization and symmetrization terms are added to generate a stable and adjoint consistent formulation allowing greater flexibility in the choice of basis functions of approximation spaces for the displacement field and the Lagrange multiplier.

After this step, stress approximations with observed optimal rates of convergence in $\mathbf{H}(\text{div})$ norm are recovered by a local post-processing of both displacement and stress using the multiplier approximation and residual forms of the constitutive and equilibrium equations at the element level.

2 The Model Problem

Let $\Omega \subset \mathbb{R}^2$ an open bounded domain with boundary $\Gamma = \partial\Omega$ and external force $\mathbf{f} \in [L^2(\Omega)]^2$. The kinematical model of linear elasticity consists in finding a displacement vector field \mathbf{u} satisfying

$$\begin{aligned} -\operatorname{div} \boldsymbol{\sigma}(\mathbf{u}) &= \mathbf{f} && \text{in } \Omega, \\ \boldsymbol{\sigma}(\mathbf{u}) &= \mathbb{D}\boldsymbol{\varepsilon}(\mathbf{u}) && \text{in } \Omega, \\ \mathbf{u} &= \mathbf{g} && \text{on } \Gamma, \end{aligned} \quad (1)$$

where $\boldsymbol{\sigma}(\mathbf{u})$ is the symmetric Cauchy stress tensor, $\boldsymbol{\varepsilon}(\mathbf{u}) = \frac{1}{2}(\nabla \mathbf{u} + \nabla \mathbf{u}^T)$ is the linear strain tensor. For linear, homogeneous and isotropic material $\boldsymbol{\sigma}(\mathbf{u})$ is given by $\boldsymbol{\sigma}(\mathbf{u}) = 2\mu\boldsymbol{\varepsilon}(\mathbf{u}) + \lambda(\operatorname{tr} \boldsymbol{\varepsilon}(\mathbf{u}))\mathbb{I}$, where $\operatorname{tr} \boldsymbol{\varepsilon}(\mathbf{u}) = \operatorname{div} \mathbf{u}$, \mathbb{I} is the identity tensor and λ and μ are the Lamé parameters.

3 Stabilized Hybrid Discontinuous Galerkin Formulation

We now present a Stabilized Hybrid Discontinuous Galerkin (SHDG) formulation for the linear elasticity problem in its primal form with the multiplier $\boldsymbol{\lambda}$ defined as the trace of \mathbf{u} : $\boldsymbol{\lambda} = \mathbf{u}|_e$ on each edge $e \in \mathcal{E}_h$.

The Stabilized Hybrid Discontinuous Galerkin (SHDG) method is formulated as:

Find the pair $[\mathbf{u}_h, \boldsymbol{\lambda}_h] \in \mathbf{V}_h \times \mathbf{M}_h$ such that, for all $[\mathbf{v}_h, \boldsymbol{\mu}_h] \in \mathbf{V}_h \times \mathbf{M}_h$

$$\begin{aligned} \sum_{K \in \mathcal{T}_h} \int_K \mathbb{D}\boldsymbol{\varepsilon}(\mathbf{u}_h) : \boldsymbol{\varepsilon}(\mathbf{v}_h) dx - \sum_{K \in \mathcal{T}_h} \int_{\partial K} (\mathbb{D}\boldsymbol{\varepsilon}(\mathbf{u}_h) \mathbf{n}_K) \cdot (\mathbf{v}_h - \boldsymbol{\mu}_h) ds \\ + \theta \sum_{K \in \mathcal{T}_h} \int_{\partial K} (\mathbb{D}\boldsymbol{\varepsilon}(\mathbf{v}_h) \mathbf{n}_K) \cdot (\mathbf{u}_h - \boldsymbol{\lambda}_h) ds \\ + \sum_{K \in \mathcal{T}_h} 2\mu \int_{\partial K} \beta_1(\mathbf{u}_h - \boldsymbol{\lambda}_h) \cdot (\mathbf{v}_h - \boldsymbol{\mu}_h) ds \\ + \sum_{K \in \mathcal{T}_h} \lambda \int_{\partial K} \beta_2((\mathbf{u}_h - \boldsymbol{\lambda}_h) \cdot \mathbf{n}_K) ((\mathbf{v}_h - \boldsymbol{\mu}_h) \cdot \mathbf{n}_K) ds \\ = \sum_{K \in \mathcal{T}_h} \int_K \mathbf{f} \cdot \mathbf{v}_h dx. \end{aligned}$$

with $\mathbf{V}_h = \{\mathbf{v} \in [L^2(\Omega)]^2 : \mathbf{v}|_K \in [S_k(K)]^2 \quad \forall K \in \mathcal{T}_h\}$,

$\mathbf{M}_h = \{\boldsymbol{\lambda} \in [L^2(\mathcal{E}_h)]^2 : \boldsymbol{\lambda}|_e = [p_l(e)]^2, \forall e \in \mathcal{E}_h^0, \boldsymbol{\lambda}|_e = \mathbf{0}, \forall e \in \mathcal{E}_h^\partial\}$,

where $S_k(K) = P_k(K)$ (the space of polynomial functions of degree at most k in both variables), and $p_l(e)$ is the discontinuous piecewise polynomial spaces of degree at most l on each edge e . The residual term multiplied by θ has been consistently added according to the following choices: $\theta = -1$, symmetric and adjoint consistent formulation; $\theta = 1$, nonsymmetric and naturally coercive formulation; and for $\theta = 0$, incomplete formulation allowing greater flexibility in the choice of basis functions of the approximation spaces for the displacement field and the Lagrange multiplier. Here, β_1 is a penalty parameter introduced to stabilize the displacement field \mathbf{u}_h and the multiplier $\boldsymbol{\lambda}_h$ and β_2 stabilizes the normal component of both variables. We also define penalty functions β_1 and β_2 as $\beta_1 = \frac{\beta_0}{h}$ and $\beta_2 = \frac{\beta_n - \beta_0}{h}$ $\forall e \in \mathcal{E}_h$ with $\beta_n > \beta_0 > 0$.

3.1 Stress and displacement local post-processing

In most engineering applications stresses are the variables of main interest. Classically, in displacement finite element for-

mulation stresses are computed indirectly using the displacement approximation and the constitutive equation only. With this classical approach, the approximation $\sigma_h = \mathbb{D}\varepsilon(\mathbf{u}_h)$ converges at best with the following rates in \mathbf{L}^2 and $\mathbf{H}(\text{div})$ norms: $\|\sigma - \sigma_h\|_{\mathbf{L}^2} = Ch^k$, $\|\sigma - \sigma_h\|_{\mathbf{H}(\text{div})} = Ch^{k-1}$.

Alternatively, we propose here a local post-processing consisting in solving at each element $K \in \mathcal{T}_h$ the local problem in stress and displacement fields:

$$\begin{aligned} -\text{div } \boldsymbol{\sigma}(\mathbf{u}) &= \mathbf{f} && \text{in } K, \\ \mathbb{A}\boldsymbol{\sigma}(\mathbf{u}) &= \boldsymbol{\varepsilon}(\mathbf{u}) && \text{in } K, \\ \mathbf{u} &= \boldsymbol{\lambda}_h && \text{on } \partial K, \end{aligned} \quad (2)$$

with $\boldsymbol{\lambda}_h$ given by the solution of the global problem and $\mathbb{A} = \mathbb{D}^{-1}$. Stress and displacement approximations $[\sigma_{PP}, \mathbf{u}_{PP}]$ for $[\sigma, \mathbf{u}]$, solution of (2), are obtained in the finite dimension spaces $\mathbb{W}_h^k(K) = \{\tau_{i,j} \in S_k(K), \tau_{i,j} = \tau_{j,i}, i, j = 1, 2\}$, $\mathbf{V}_h^k(K) = \{\mathbf{v}_i \in S_k(K), i = 1, 2\}$. Considering the following residual form on each element $K \in \mathcal{T}_h$

$$\begin{aligned} \int_K \mathbb{A}\boldsymbol{\sigma}_{PP} : \boldsymbol{\tau}_h dx + \int_K \mathbf{u}_{PP} \cdot \text{div} \boldsymbol{\tau}_h dx - \int_{\partial K} \boldsymbol{\lambda}_h \cdot \boldsymbol{\tau}_h \mathbf{n}_K ds \\ + \int_K \text{div} \boldsymbol{\sigma}_{PP} \cdot \mathbf{v}_h dx + \int_K \mathbf{f} \cdot \mathbf{v}_h dx \\ + \delta_1 \int_K (\mathbb{A}\boldsymbol{\sigma}_{PP} - \boldsymbol{\varepsilon}(\mathbf{u}_{PP})) : (\boldsymbol{\tau}_h - \mathbb{D}\boldsymbol{\varepsilon}(\mathbf{v}_h)) dx \\ + \frac{\delta_2}{2\mu} \int_K (\text{div} \boldsymbol{\sigma}_{PP} + \mathbf{f}) \cdot \text{div} \boldsymbol{\tau}_h dx + 2\mu \int_{\partial K} \beta_1 (\mathbf{u}_{PP} - \boldsymbol{\lambda}_h) \cdot \mathbf{v}_h ds \\ + \lambda \int_{\partial K} \beta_2 ((\mathbf{u}_{PP} - \boldsymbol{\lambda}_h) \cdot \mathbf{n}_K)(\mathbf{v}_h \cdot \mathbf{n}_K) ds = 0. \end{aligned}$$

For appropriate choices of the stabilization parameters δ_1 and δ_2 , we have observed the following convergence rate for the post-processed stress:

$$\|\sigma - \sigma_{PP}\|_{\mathbf{H}(\text{div})} = Ch^k \quad (3)$$

which is one order higher.

4 Numerical Results

The performance of the method is tested for a plane-strain problem, defined on square domain $\Omega = (0, 1) \times (0, 1)$ with homogeneous boundary conditions, considering the elasticity modulus $E = 1$ and forcing term:

$$f_1(x, y) = (2\nu(2\mu + \lambda) - (\mu + \lambda)) \sin(\pi x) \cos(\pi y) \quad (4)$$

$$f_2(x, y) = (2\nu(2\mu + \lambda) - (3\mu + \lambda)) \sin(\pi y) \cos(\pi x) \quad (5)$$

such that the exact solution is given by

$$u_1(x, y) = \frac{\nu}{\pi^2} \sin(\pi x) \cos(\pi y) \quad (6)$$

$$u_2(x, y) = \frac{(\nu - 1)}{\pi^2} \cos(\pi x) \sin(\pi y). \quad (7)$$

Results of a study on the h -convergence for displacement (\mathbf{u}_h) and stresses (σ_h) are presented in Figs. 1–2. In these experiments we use uniform partitions of the domain, symmetric formulation ($\theta = -1$), linear triangular elements with $k = l = 1$, $\beta_0 = 2$ and $\beta_n = 7$. Figure 1 shows optimal rates of convergence for displacement (\mathbf{u}_h) in L^2 norm and H^1 seminorm, respectively with identical accuracy for all approximations when $\nu \rightarrow 1/2$. In Figure 2 we have a comparison between the stress recovered by using the constitutive law and the local postprocessing formulation. It is seen that when we use the consti-

tutive law the locking effect appears, but using the proposed formulation optimal rates are obtained.

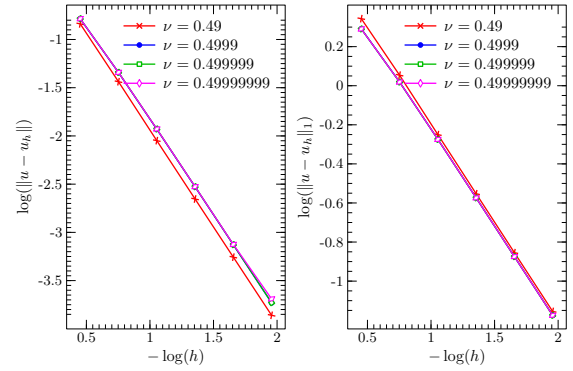


Figure 1: Convergence study for \mathbf{u}_h in (a) $L^2(\Omega)$ norm and (b) $H^1(\Omega)$ seminorm of SHDG approximations with discontinuous multiplier, $\beta_0 = 2$, $\beta_n = 7$, $\delta_1 = 40$ and $\delta_2 = -1/2$.

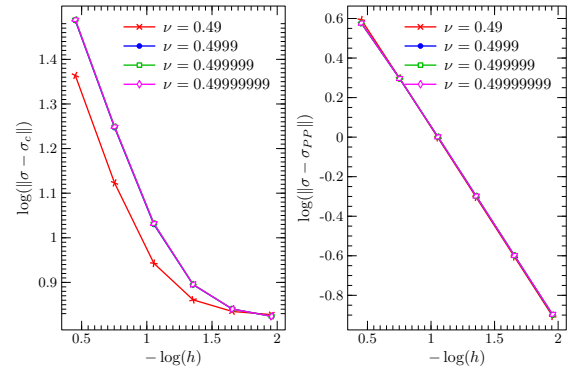


Figure 2: Convergence study for σ in $H(\text{div})$ norm of SHDG approximations with discontinuous multiplier, $\beta_0 = 2$, $\beta_n = 7$, $\delta_1 = 40$ and $\delta_2 = -1/2$.

5 Conclusions

The Hybrid methods preserve the main properties of the DG method but with reduced computational cost. Is easily implemented using the same data structure of continuous Galerkin methods. Numerical results show optimal rates of convergence for the primal variable \mathbf{u}_h and for the Lagrange multiplier $\boldsymbol{\lambda}_h$. A local post-processing based on the multiplier approximation and residual forms of the constitutive and equilibrium equations at the element level is proposed to recover stress approximations with observed optimal rates of convergence in $\mathbf{H}(\text{div})$ norm.

References

- [1] C. O. Faria, A. F. D. Loula, and A. J. B. dos Santos. Primal Stabilized Hybrid and DG finite element methods for the linear elasticity problem. *Computers and Mathematics with Applications*, 68:486–507, 2014.
- [2] Cristiane O. Faria, Abimael F.D. Loula, and Antônio J.B. dos Santos. Stabilized hybridized finite element method for incompressible and nearly incompressible elasticity. *XXXIV Congresso Ibero Latino Americano de Métodos Computacionais em Engenharia (XXXIV CILAMCE)*, 2013. 10–13 de novembro, Pirenópolis – GO, Brasil.



EXPLICIT RESOLUTION BY LINEAR FINITE ELEMENTS OF A SYSTEM WHICH DESCRIBES EVOLUTIVE VISCOELASTIC FLOWS

Author: Patricia Dias Gomes¹ patriciadiasgomes@gmail.com
Advisor(s): José Henrique C. Araújo¹

¹ Institute of Computation / UFF

May 6, 2015

PPG-EM Seminars: season 2015
www.ppg-em.uerj.br

Keywords: FEM; viscoelastic flow.

3 Time Discretization and Splitting Algorithm

1 Introduction

A three-field finite element scheme designed for solving systems of partial differential equations governing stationary incompressible flows is presented. It is based on the simulation of a time-dependent behavior. Once a classical time-discretization is performed, the resulting three-field system of equations allows for a stable approximation of velocity, pressure and extra stress tensor, by means of continuous piecewise linear finite elements, in both two- and three-dimension space. The main advantage of this formulation is the fact that it implicitly provides an algorithm for the iterative resolution of system non-linearities. We show that it can be employed with advantages, to the case of newtonian or quasi-newtonian fluids.

2 Generalized Stokes System

We introduce our methodology in the context of the following generalized Stokes system, derived from the linearization of the equations that govern the flow of a Maxwell viscoelastic liquid, assuming moderate velocities and velocity gradients, the non linear terms may be neglected, namely:

From a given state at time $t = 0$ defined by a given solenoidal velocity \mathbf{u}^0 and an extra stress tensor σ^0 , for $t > 0$ find p, \mathbf{u}, σ that solve the following system, with $\mathbf{u} = \mathbf{g}$ on $\partial\Omega \times (0, \infty)$:

$$\left. \begin{aligned} \frac{\partial \mathbf{u}}{\partial t} - \nabla \cdot \sigma + \nabla p &= \mathbf{f} \\ \nabla \cdot \mathbf{u} &= 0 \\ \sigma + \lambda \frac{\partial \sigma}{\partial t} &= 2\eta D(\mathbf{u}) \end{aligned} \right\} \text{in } \Omega \times (0, \infty). \quad (1)$$

We present an algorithm for solving both newtonian and non newtonian flow equations, in the \mathbf{u}, p, σ formulation. Although this algorithm and the underlying variational formulation are described here only in the context of problem (1), its adaption to more general cases is straightforward, including for instance the Navier-Stokes equations, or yet turbulent flow with turbulent stress models. Indeed in the latter cases it suffices to take $\lambda = 0$, before incorporating non linear expressions or terms. It seems however that in the context of viscoelastic flow the new approach appears to be the most promising, since in this case the use of a three-field formulation is mandatory.

We have mainly dealt with an explicit splitting algorithm for the time integration or the iterative solution of system (1). However before presenting it we consider the underlying implicit discretization in time of (1).

Let $\Delta t > 0$ be a given time step. Then starting from \mathbf{u}^0 and σ^0 , for $n = 1, 2, \dots$, and prescribing $\mathbf{u}^n = \mathbf{g}$ on $\partial\Omega$ for every n , we determine approximations of $p(n\Delta t)$, $\mathbf{u}(n\Delta t)$ and $\sigma(n\Delta t)$, denoted by p^n , \mathbf{u}^n and σ^n respectively, as the solution of the following problem:

$$\left. \begin{aligned} \frac{\mathbf{u}^n - \mathbf{u}^{n-1}}{\Delta t} - \nabla \cdot \sigma^n + \nabla p^n &= \mathbf{f} \\ \nabla \cdot \mathbf{u}^n &= 0 \\ \sigma^n + \lambda \left(\frac{\sigma^n - \sigma^{n-1}}{\Delta t} \right) &= 2\eta D(\mathbf{u}^n) \end{aligned} \right\} \text{in } \Omega. \quad (2)$$

4 Space Discretization

Once we held the demonstration of equivalence between the time discretized system and the chosen variational

formulation, we proceed then to the space discretization of the system. This was performed with linear finite element for the three fields u , p , σ and regularity assumptions in respect of the domain and the spaces (cf. [1]). Once we have obtained the fully discretized system, we consider a lumped mass version of system, denoted by $(\cdot)_h$, which diagonalizes weighted mass matrices. Next we consider the internal iteration algorithm to explicitly solve the system in every time step, with respect to each velocity and extra stress tensor components. As can be observed in the system (3), s is a index of internal iteration. It is intended to perform an approximation as closer as possible between the solution of the explicit scheme and the solution of the implicit scheme when s tends to infinity.

$$\left\{ \begin{array}{l} \Delta t^2(\nabla p_h^{n,s}, \nabla q) = \Delta t^2[(\mathbf{f}_h^n, \nabla q) + (\nabla \cdot \sigma_h^{n,s-1}, \nabla q)] \\ + \Delta t(\mathbf{u}_h^{n-1}, \nabla q) - \Delta t < \mathbf{g}_h^n, q\nu >_{1/2, \Gamma} \forall q \in Q_h \\ \\ (\mathbf{u}_h^{n,s}, \mathbf{v})_h = \Delta t(\mathbf{f}_h^n + \nabla \cdot \sigma_h^{n,s-1} - \nabla p_h^{n,s}, \mathbf{v}) + \\ (\mathbf{u}_h^{n-1}, \mathbf{v})_h \quad \forall \mathbf{v} \in V_h \\ \\ \frac{\lambda + \Delta t}{2\eta}(\sigma_h^{n,s}, \tau)_h = \frac{\lambda}{2\eta}(\sigma_h^{n,s-1}, \tau)_h - \Delta t^2(\mathbf{f}_h^n \\ + \nabla \cdot \sigma_h^{n,s-1} - \nabla p_h^{n,s}, \nabla \cdot \tau) - \Delta t[(\mathbf{u}_h^{n-1}, \nabla \cdot \tau) \\ - < \mathbf{g}_h^n, \tau\nu >_{1/2, \Gamma}] \quad \forall \tau \in \Sigma_h \end{array} \right. \quad (3)$$

5 Numerical Results

In order to check the accuracy of our method (3), we performed error estimates to some three-dimensional problems. We present one particular case of (1) with known exact solution presented in section 5.3 in [1]. More specifically, we solved the system of equations (3) in the domain $\Omega \times (0, T)$, Ω being the unit cube $(0, 1)^3$ and $T = 1$, subject to volumetric force \mathbf{f} and defined initial and boundary conditions. We solved this problem with uniform tetrahedral meshes obtained by first subdividing into M^3 equal cubes with edge length $h = 1/M$, each one of them being in turn subdivided

into six tetrahedra in a classical manner. The figure 1 displays approximate relative errors for velocity, pressure and extra stress tensor in the standard L^2 -norm for different values of M with $t = 1$, $\lambda = 10$, $\eta = 1$, and Δt taken equal to $h/50$.

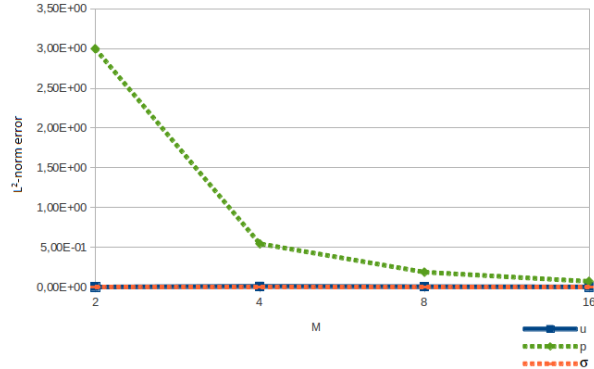


Figure 1: L^2 -norm relative errors for $\lambda = 10$, $\eta = 1$ and $t = 1.0$

6 Conclusions

- Widespread simplifying assumption of Oldroyd-like fluid avoided;
- Convergence results derived even for the pressure;
- In practice explicit stable scheme for $\Delta t = O(h)$;
- Code adaption to treat Oldroyd fluids;
- Application to thixotropic models for jelly-like fluids;
- Extending convergence analysis to complete non-linear system;

References

- [1] P. Gomes. *Resolução Explícita por Elementos Finitos do Sistema que Descreve Escoamentos Evolutivos Viscoelásticos*. Phd thesis, UFF, Rio de Janeiro - RJ, 2015.

UNCERTAINTIES IN PHYSICAL SYSTEMS: WHY TO QUANTIFY AND HOW TO MODEL?

Author: Americo Cunha Jr¹ americoc@ime.uerj.br

¹ Universidade do Estado do Rio de Janeiro

June 3, 2015

PPG-EM Seminars: season 2015
www.ppg-em.uerj.br

1 Introduction

Computational models has been increasingly used in sciences and engineering for design and analysis of complex physical systems. This increase has taken place due to the versatility and low cost of a numerical simulation compared to an approach based on experimental analyzes on a test rig. However, any computational model is subject to a series of uncertainties, due to variabilities on its parameters and, mainly, because of assumptions made in the model conception that may not be in agreement with reality [4]. The first source of uncertainty is inherent limitations in measurement processes, manufacturing, etc., while the second source is essentially due to lack of knowledge about the phenomena observed in the physical system. Also, an increasingly frequent requirement in several projects of engineering is the robust design of a component, i.e., with low sensitivity to the variation of a certain parameter, and this requires the quantification of model uncertainties. In this short work it will exposed some fundamental notions related to the quantification of uncertainties in physical systems, and it will be illustrated the construction of a probabilistic model for uncertainties description in a simplistic mechanical system.

2 Uncertainties, variabilities and errors

To fix ideas, consider a designed system, which will give rise to a real system through a manufacturing process. This manufacturing process is subject to a series of variabilities (due to differences in the geometric dimensions of the components, variations in operating conditions, etc) that result in some differences in the parameters (geometrical dimensions, physical properties, etc) of two or more real systems manufactured. The inaccuracies on these parameters is known as *data uncertainty* [4, 5].

In order to make predictions about the behavior of the physical system, a computational model should be used. In the conception this model mathematical hypotheses are made. These considerations may be or not in agreement with the reality and should introduce additional inaccuracies in the model, known as *model uncertainty*. This source of uncertainty is essentially due to lack of knowledge about the phenomenon of interest and, usually, is the largest source of inaccuracy in model response [4, 5].

A schematic representation of the conceptual process which show how uncertainties of a physical system are introduced into a computational model is shown in Figure 1.

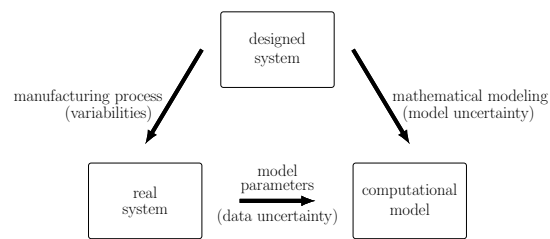


Figure 1: Representation showing how uncertainties are introduced into a computational model.

Uncertainties affect the response of a computational model, but should not be considered errors because they are physical in nature. Errors in the model response are due to the discretization process of the equations, to the use of finite precision arithmetic to perform the calculations, and possible bugs during the computer code implementation

Therefore, unlike the uncertainties, that have physical origin, errors are purely mathematical in nature, and can be controlled if the numerical methods and algorithms used are well known by the analyst.

3 Frameworks for uncertainties description

Being uncertainties in the physical system the focus of stochastic modeling, two approaches are found in the scientific literature for the treatment of uncertainties: (i) *non-probabilistic*, and (ii) *probabilistic*.

The non-probabilistic approach uses techniques such as interval and fuzzy finite elements; imprecise probabilities; evidence theory; probability bounds analysis; fuzzy probabilities; etc, and is generally applied only when the probabilistic approach can not be used [1].

The probabilistic approach uses probability theory to model the uncertainties of the physical system as random mathematical objects. This approach has a more well-developed and consistent mathematical framework, and, for this reason, there is a consensus among the experts that it is preferable whenever possible to use it [2, 5].

4 A simplistic stochastic mechanical system

Consider the simplistic mechanical system shown in Figure 2, which the spring extreme displacement is given by $u = k^{-1}f$.

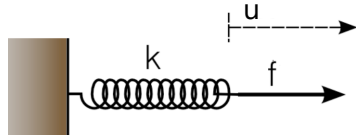


Figure 2: A spring subjected to a force.

If the spring stiffness is uncertain the system response is also subject to uncertainties. Representing the stiffness the random variable K , the spring displacement is now the random variable $U = K^{-1}f$.

Note that, to compute any statistical information of U , such as the mean value

$$\mathbb{E}\{U\} = \int_{\mathbb{R}} k^{-1} f p_K(k) dk, \quad (1)$$

it is necessary to know the *probability density function* of K , denoted by $p_K(k)$.

5 Specifying probability distributions

In order to obtain a consistent stochastic model, one cannot arbitrarily choose the probability distribution of a random parameters, under the penalty of violating some physical principle and/or obtain an inconsistent mathematical model. It is a consensus that all information available about these parameters must be taken into account before define their distributions, i.e., specify their PDFs [4].

Accordingly, the *maximum entropy principle* can be used to obtain a desired PDF.

Among all the probability distributions, consistent with the current known information of a given random parameter, the one which best represents your knowledge about this random parameter is the one which maximizes its entropy:

$$S(p_K) = - \int_{\mathbb{R}} p_K(k) \ln p_K(k) dk. \quad (2)$$

Assuming the following information is known about K :

- $\text{Supp } p_K \subset (0, +\infty) \implies K > 0 \text{ a.s.}$
- $\mathbb{E}\{K^2\} < +\infty$
- $\mathbb{E}\{K\} = m$ is known

- $\mathbb{E}\{K^{-2}\} < +\infty$,

it can be shown that the *gamma distribution*

$$p_K(k) = \mathbf{1}_{(0,+\infty)}(k) \frac{1}{m} \frac{\delta^{-2\delta^{-2}}}{\Gamma(\delta^{-2})} \left(\frac{k}{m}\right)^{\delta^{-2}-1} \exp\left\{-\frac{k/m}{\delta^2}\right\},$$

with mean m and dispersion parameter δ , is the probability distribution that maximizes the entropy, respecting the known statistical information on the parameter K [3].

To the best of the authors knowledge, the distribution obtained this way is the one that most accurately describes the current knowledge about the random parameter K .

6 Conclusions

In this short paper are presented some fundamental notions related to the quantification of uncertainties in physical systems and it is illustrated the construction of a probabilistic model for uncertainties description in a simplistic mechanical system.

7 Acknowledgments

The authors is indebted to Brazilian agencies CNPq, CAPES, and FAPERJ for the financial support given to this research.

References

- [1] D. Moens and M. Hanss. Non-probabilistic finite element analysis for parametric uncertainty treatment in applied mechanics: Recent advances. *Finite Elements in Analysis and Design*, 47:4–16, 2011. doi: 10.1016/j.fin.2010.07.010.
- [2] G. I. Schuëller. A state-of-the-art report on computational stochastic mechanics. *Probabilistic Engineering Mechanics*, 12:197–321, 1997. doi: 10.1016/S0266-8920(97)00003-9.
- [3] C. Soize. Short course on Uncertainties and Stochastic Modeling. PUC-Rio, 4-7 August 2008.
- [4] C. Soize. *Stochastic Models of Uncertainties in Computational Mechanics*. American Society of Civil Engineers, Reston, 2012.
- [5] C. Soize. Stochastic modeling of uncertainties in computational structural dynamics — recent theoretical advances. *Journal of Sound and Vibration*, 332:2379–2395, 2013. doi: 10.1016/j.jsv.2011.10.010.



APPLICATION OF FINITE ELEMENT METHODS (FEM) IN THE STUDY OF REACTIVE FLOWS

Author: Alcéstes G. de Oliveira Filho¹ ade_oliveira@hotmail.com
Advisor(s): Norberto Mangiacapchi¹

¹ State University of Rio de Janeiro

June 10, 2015

PPG-EM Seminars: season 2015
www.ppg-em.uerj.br

Keywords: Finite Element Method, Reactive flows

1.4 Specific situations under consideration

- Determination of species concentration profiles in tubular reactors, where inlet and outlet concentrations of the reactants are constant;
- Determination of species concentration profiles in tubular reactors, where the inlet concentrations are transient and the outlet condition represents a condition of physical-chemical equilibrium;
- Determination of pollutants concentration profiles in waterways, with inlet transient condition and an outlet condition that represents a physical-chemical balance.

1 Introduction

1.1 Purpose

To develop prototype computer codes that could allow the mastering of techniques involved in the implementation of FEM to reactive flows.

1.2 Motivation

CH₄ generation from biomass on the bottom of hydroelectric reservoirs, their release in the atmosphere and their potential negative effects as greenhouse gas.

1.3 General description

The construction of large dams to meet the growing energy needs of the country has always been primarily considered due to the fact that very active environmental pressure groups consider this option as being more "clean" and safe than the thermoelectric generation. In reality, the hydropower plants also provide large environmental impact, which can be even more significant than the thermoelectric option because the anaerobic decomposition of organic matter, generating large volumes of greenhouse gases, mainly methane, further exacerbating the problem of global warming. In preparation for a main study, FEM is being used for the numerical investigation of reactive flows in 1D and 2D with application in determination of concentration profiles of chemical species in continuous tubular reactors and degradable pollutants in watercourses. The problem is being studied by solving the transport equation subjected to transient boundary conditions, as it would involve the operation of chemical reactors in diversified production and non-uniform pollutants discharge. By keeping the problem within certain parameters, it was possible to achieve the implementation of a scheme involving the usual spatial discretization for GFEM and Crank-Nicholson for temporal derivative, conveniently dealing with the problems of stability, and a new approach to treat a natural boundary condition.

2 Numerical techniques

The method has been applied in accordance with the Galerkin model and the resulting integrals of weak formulation were evaluated by the Gaussian Quadrature. The programs generated structured triangular and square meshes. The results were checked with one-dimensional analytical solutions available.

Experimentation with the material derivative as boundary condition at the outlet, i.e.,

$$\left[\frac{\partial C(x_i, t)}{\partial t} + \bar{u}_{x_i} \frac{\partial C(x_i, t)}{\partial x_i} \right]_{\Gamma_{\text{out}}} = 0 \quad (1)$$

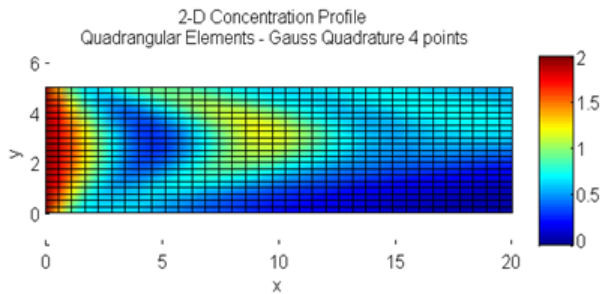
Which is equivalent to the weak form as follows:

$$\begin{aligned} & \sum_{j=1}^{NN} \left(\int_{\Omega} S_i S_j d\Omega + \frac{D}{U} \int_{\Gamma} S_i S_j d\Gamma \right) \frac{dC_j}{dt} + \\ & + \sum_{j=1}^{NN} \int_{\Omega} S_i \left(\bar{u}_x \frac{\partial S_j}{\partial x} + \bar{u}_y \frac{\partial S_j}{\partial y} \right) d\Omega C_j + \\ & + \sum_{j=1}^{NN} \int_{\Omega} \left(D_x \frac{\partial S_i}{\partial x} \frac{\partial S_j}{\partial x} + D_y \frac{\partial S_i}{\partial y} \frac{\partial S_j}{\partial y} \right) d\Omega C_j + \\ & + \sum_{j=1}^{NN} \int_{\Omega} k S_i S_j d\Omega C_j = 0 \end{aligned} \quad (2)$$

This implies in a modified mass matrix, first term on

the left, corrected by the boundary surface integral, and a stiffness matrix modified by the term of reaction, i.e.,

$$[\mathbf{M}_1] \{\dot{\mathbf{C}}\} + [\mathbf{K}_1] \{\mathbf{C}\} = 0 \quad (3)$$



4 Conclusion

For its solution, Crank-Nicolson Method and existing criteria to address possible instabilities are applied.

3 Results

The following figure shows an example of a reactive flow simulation with two-dimensional fully developed parabolic speed profile, obtained with boundary condition given by eq.1.

The use of FEM is feasible to develop models that can simulate chemical species concentration profiles in reactive flows. The Material Derivative as balancing condition on outlet, represent more faithfully the physical problem and does not induce greater instability. The application of these models in the simulation of the evolution of methane from the bottom of reservoirs of hydroelectric plants can provide ways to capture this gas on the surface and mitigate adverse environmental effects.



SOLUTION OF THE INCOMPRESSIBLE NAVIER-STOKES EQUATIONS BY PROJECTION METHODS USING THE INTEGRAL TRANSFORM TECHNIQUE

Author: Daniel J. N. M. Chalhub¹ daniel.chalhub@uerj.br

¹ State University of Rio de Janeiro

July 1, 2015

PPG-EM Seminars: season 2015
www.ppg-em.uerj.br

Keywords: Incompressible Navier-Stokes, Hybrid Analytic-Numerical Methods, Integral Transform Technique, Projection Methods

1 Introduction

The major difficulty for the numerical simulation of incompressible flows is that the velocity and pressure are coupled by the incompressibility constraint. To overcome this difficulty in time dependent viscous incompressible flows, fractional step methods, which are also referred in the literature as projection methods, were developed. The major computational time associated with these schemes is the solution of the Poisson equation at each step, which consumes large amounts of computer time. One reason for this is that the convergence rate of iterative methods that are commonly used for this purpose, such as the Jacobi and Gauss-Seidel, rapidly decreases as the mesh is refined [7].

On the other hand, in the realm of analytical methods, the Integral Transform Technique [4] has been playing a big role. It deals with expansions of the sought solution in terms of infinite orthogonal basis of eigenfunctions, keeping the solution process always within a continuous domain. The resulting system is generally composed of a set of uncoupled differential equations which can be solved analytically. However, a truncation error is involved since the infinite series must be truncated to obtain numerical results. This error decreases as the number of summation terms (truncation order) is increased, and the solution converges to a final value. Due to the series representation nature of the Integral Transform Technique, the estimated error can be easily obtained, which results in better global error control of the solution. The disadvantage associated with this approach is the need for more elaborate analytical manipulation. This effort can be greatly minimized with the use of symbolical computation.

Recent works of Chalhub et al. [2, 1] introduced the idea of a semi-analytical solution for the poisson equation arising from the incompressible Navier-Stokes equations.

2 Classical Projection Method

In order to solve an in compressible flow problem, one needs to solve the incompressible Navier-Stokes equations. A more efficient way to solve these equations was introduced by Chorin [3] as Projection Methods. The key advantage of the projection method is that the computations of the velocity and pressure fields are decoupled. The algorithm of projection method is based on the Helmholtz-Hodge decomposition¹ [8] of any vector field into a solenoidal part and an irrotational part.

3 Solution of the Pressure Poisson Equation

The general Poisson equation for pressure in two-dimensions, using cartesian coordinates and compatible boundary conditions can be written in the following form:

$$\frac{\partial^2 p}{\partial x^2} + \frac{\partial^2 p}{\partial y^2} = Q(x, y, t) \quad (1)$$

where Q is the source term.

Due to the Navier-Stokes nature, Neumann boundary conditions are used for the pressure.

3.1 Filtering Scheme for Integral Transformation

Before continuing to the solution via integral transformation, it is proposed a separation of the pressure on the following form:

$$p(x, y, t) = p^*(x, y, t) + p_f(x, y) \quad (2)$$

where p^* is the filtered pressure and p_f is a known filter function.

4 Classical Integral Transform Technique: Single Transformation

In this work the Classical Integral Transform Technique [4] is used for the purpose of solving the filtered Poisson equation. This is an analytical technique that uses expansions of the sought solution in terms of an infinite orthogonal basis of eigenfunctions, keeping the

¹Also known as Helmholtz decomposition and theorem of Ladyzhenskaya

solution process always within a continuous domain. In order to establish the transformation pair, the pressure field is written as function of an orthogonal eigenfunctions obtained from an auxiliary eigenvalue problem known as the Helmholtz classic problem in cartesian coordinates [4].

5 Results

In this chapter the results obtained from the computational code developed using the new formulation will be presented. The solution of the incompressible flow in a test case simulated by the proposed method will be presented. The codes were implemented in FORTRAN 90 using GFortran, they were compiled in serial computation and using the -O3 optimization flag.

The solution of the classic Lid-Driven Cavity problem is shown to validate the proposed formulation and evaluate its performance for more demanding problems. Three methods are computed and evaluated: CITT using single transformation with filtering scheme (CITT-ST-F), CITT using single transformation without filtering scheme (CITT-ST) and a code developed using Finite Volumes Methods (FVM) [6] together with a Gauss-Seidel linear system solver [5].

In figure 1 presents the total computational time required to achieve steady state versus mesh size. It can be seen that CITT-ST without filter requires a lot more computational time compared to the other methods. For very coarse meshes, CITT-ST-F and FVM require approximately the same computational time, however, when the mesh is refined, CITT-F overcomes FVM performance.

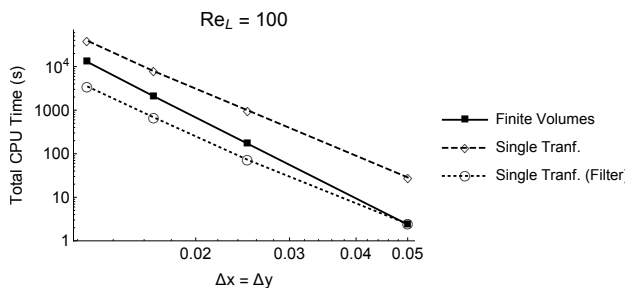


Figure 1: Lid-Driven Cavity: Total computational time consumed to achieve steady state.

For the computation, all results were calculated with prescribed relative precision of 10^{-6} for the Gauss-Seidel iterative solver used in FVM and also for the CITT summation series convergence. In order to guarantee this precision in the truncated summations, an automatic truncation procedure was developed and implemented. The projection method was used and the time-steps Δt utilized were the same for all methods. The results computed in the current work were carried out using only uniform meshes and also considering $\Delta x = \Delta y$ and the Neumann boundary conditions for pressure on all impermeable/no slip walls were approximated to zero

without violating the Poisson-Neumann compatibility condition.

6 Conclusions

The present work developed a numerical method for solving the unsteady incompressible Navier-Stokes equations with primitive variables in two dimensions, although it can be easily extended to tree dimensions. The novel methodology is based on projection methods schemes using a mixed approach through the Integral Transform Technique. The Lid-Driven Cavity problem was analysed. Results showed a very similar qualitative behavior. One could see that for very poorly refined meshes CITT-ST-F and FVM had similar performances. However for more refined meshes, CITT-ST-F had a dramatically better performance and CITT-ST (without filter) had the worst performance overall. Although more investigations are needed, CITT-ST-F has a great potential of being a good substitute for the methodologies currently used to solve the pressure Poisson equation.

References

- [1] D. J. M. N. Chalhub, L. A. Sphaier, and L. S. de B. Alves. Hybrid solution scheme for the discrete pressure poisson equation using integral transformation. In *15th Brazilian Congress of Thermal Sciences and Engineering (ENCIT2014)*, Belem, PA, Brazil, 2014.
- [2] Daniel J. N. M. Chalhub, Leandro A. Sphaier, and Leonardo S. de B. Alves. Integral Transform Analysis of Poisson Problems that Occur in Discrete Solutions of the Incompressible Navier-Stokes Equations. *Journal of Physics: Conference Series*, 547 (1):012040, November 2014. ISSN 1742-6596.
- [3] A. J. Chorin. Numerical solution of the Navier-Stokes equations. *Mathematics of Computation*, 22: 745–762, 1968.
- [4] M. D. Mikhailov and M. N. Özişik. *Unified Analysis and Solutions of Heat and Mass Diffusion*. John Wiley & Sons, New York, 1984.
- [5] P. Moin. *Fundamentals of Engineering Numerical Analysis*. Cambridge University Press, New York, NY, 2001.
- [6] Suhas V. Patankar. *Numerical Heat Transfer and Fluid Flow*. Hemisphere, 1980.
- [7] H. K. Versteeg and W. Malalasekera. *An Introduction to Computational Fluid Dynamics, The Finite Volume Method*. Pearson Prentice Hall, Harlow, England; New York, 2nd edition, 2007.
- [8] Jie-Zhi Wu, Hui-yang Ma, and M.-D. Zhou. *Vorticity and Vortex Dynamics*. Springer Science & Business Media, April 2007. ISBN 9783540290285.



NUMERICAL MODELLING OF TWO-PHASE FLOWS WITH MOVING CONTACT LINES

Author: Erik Gros¹ erik.gros@epfl.ch
Advisors: John R. Thome¹; Gustavo R. Anjos²

¹ Ecole Polytechnique Federale de Lausanne, Heat and Mass Transfer Laboratory

² Rio de Janeiro State University (UERJ)

August 19, 2015

PPG-EM Seminars: season 2015
www.ppg-em.uerj.br

Keywords: Moving contact lines; two-phase flow.

Abstract. Numerical simulation is employed to simulate two-phase flow phenomena using the continuum method for surface tension modeling. The set of equations are based on the 'one-fluid' Arbitrary Lagrangian-Eulerian (ALE) description of the Navier-Stokes equations. These equations are discretized by the Finite Element method on an unstructured mesh in which the phase boundary is represented by a set of interconnected elements that are part of the computational mesh, thus a sharp representation is successfully achieved. The presented modeling will then be used to investigate two-phase flows with moving contact lines, slug and annular flows in microchannels. These problems are of great interest for technology applications such as the cooling of microelectronic devices. The employed formulation, the interface representation, bubble-wall modeling and some initial results of this Ph.D. thesis will be presented for 2-dimensional cartesian and axisymmetric cylindrical coordinates.

1 Introduction

Flows with two unmixable fluid phases are commonly found in many practical applications, such as in refrigeration industry or in cooling systems of the next generation of microelectronic devices. In the latter small scales make quantitative experimental data difficult to obtain. Numerical simulations offer an alternative approach, complementing the experimental and theoretical ones. A well established method to model fluid flow with different phases computationally is the so called one fluid formulation, where a single set of equations is used to describe the entire flow field. The effects of surface tension, which occur only at the interface between two fluids can be modelled by a volume force as proposed by [2]. Different approaches exist to describe the motion of the interface. Eulerian methods where the computational mesh is fixed and the interface is described by the advection of a scalar field. Lagrangian

methods which use a mesh moving with the flow. In this work a one fluid formulation is employed and the interface is tracked in a Lagrangian way.

Contact lines may appear in two-phase flows whenever an interface intersects with a solid boundary. Such as when a drop of liquid is placed on a surface under the influence of gravitational field. Despite its occurrence in many important applications and in everyday life contact line motion is still not physically understood.

2 Governing Equations

The Navier-Stokes equations for two-phase flow in 2d cartesian ($m = 0$) or axisymmetric cylindrical coordinates ($m = 1$) read

$$\rho \frac{\partial v_x}{\partial x} + \frac{\partial v_r}{\partial r} + m \frac{v_r}{r} = 0,$$

$$\begin{aligned} \rho \frac{D v_x}{D t} &= -\frac{\partial p}{\partial x} + \mu \Delta v_x + \rho g + f_x, \\ \rho \frac{D v_r}{D t} &= -\frac{\partial p}{\partial r} + \mu \left(\Delta v_r - m \frac{v_r}{r^2} \right) + f_r. \end{aligned}$$

Use has been made of the operator

$$\Delta = \frac{\partial^2}{\partial x^2} + \frac{\partial^2}{\partial r^2} + \frac{m}{r} \frac{\partial}{\partial r}.$$

To not interfere with the symmetry it has been assumed that gravity acts only in the direction of the symmetry axis (x -direction). The body force term $\vec{f} = (f_x, f_r)^T$ accounts for the effects of surface tension modeled by [2]

$$f = \sigma \kappa \vec{n} \delta$$

where σ is the surface tension coefficient and δ is the Dirac distribution with support on the interface. The normal vector \vec{n} and the mean curvature κ are defined by the geometry of the interface. The curvature is

computed by

$$\kappa_{axi} = \kappa_{2d} + m \frac{\sin(\phi)}{r}$$

where κ_{2d} is the curvature of the interface in the 2d-plane and ϕ is the angle of the interface normal relative to the symmetry axis, see Fig 1.

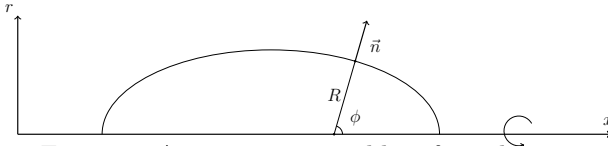


Figure 1: Axisymmetric problem formulation.

3 Mesh Description

In this work an arbitrary Lagrangian Eulerian (ALE) method is employed. This method combines the Lagrangian description (moving mesh) with the Eulerian description (fixed mesh). It makes use of boundary-adapted grids, where the mesh nodes at the interphase are moved along with the flow velocity in Lagrangian fashion while the boundary nodes remain fixed in Eulerian fashion. To ensure a good quality mesh at any time, points can be deleted, added and displaced to the mesh and the solution interpolated on the new mesh. More details regarding the computational method can be found in [1].

4 Results

In this section we describe a numerical approach to moving contact lines, which consists in imposing a static (constant) contact angle at the three phase contact line. Such an approach is widely used in literature, see e.g. [3]. The model problem consists in a liquid drop released on a surface and surrounded by a lighter liquid or a gas. The flow is modelled in the 2d (cartesian) plane. At the beginning the drop is half-circular and a fixed value of the contact angle θ is imposed at all times. The drop deforms due to gravity which is directed downward and also as a consequence of the imposed contact angle. At steady state, the shape of the drop is given by the

balance of two forces: the gravitational force which tries to spread the drop on the surface minimizing its potential energy and the surface tension which tries to minimize the drop's surface. The ratio of these two forces is described by the Eotvos number

$$Eo = \frac{\rho_l g R_0^2}{\sigma}$$

based on the initial radius R_0 of the drop and the density of the liquid ρ_l . In the absence of gravity, that is for $Eo = 0$, the drop's shape at steady state is a circular-cap. The simulation results for a case dominated by gravity ($Eo = 10$), with an imposed contact angle of 50° , can be seen in Fig. 2.

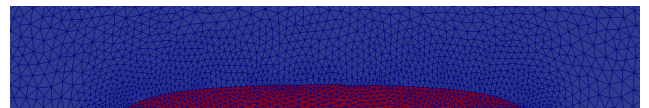


Figure 2: Final bubble shape for $Eo = 10$ and $\theta = 50^\circ$.

5 Conclusions and Further Work

In this article a numerical framework for axisymmetric simulations and static contact angles has been presented. Validations of the already implemented features namely static contact angle, phase change, annular flows will be performed. Afterwards, additional phenomena such as dynamic contact angles and Navier-Slip boundaries will also be developed.

References

- [1] G.R. Anjos, N. Borhani, N. Mangiacavalli, and Thome J.R. A 3d moving mesh finite element method for two-phase flows. *Journal of Computational Physics*, 270:366–377, 2014.
- [2] J.U. Brackbill, D.B. Kothe, and Zemach C. A continuum method for modeling surface tension. *Journal of Computational Physics*, 100:335–354, 1992.
- [3] J.-B. Dupont and D. Legendre. Numerical simulation of static and sliding drop with contact angle hysteresis. *Journal of Computational Physics*, 229: 2453–2478, 2010.



COUNTER-CURRENT THERMOCAPILLARY MIGRATION OF BUBBLES IN MICROCHANNELS USING SELF-REWETTING LIQUIDS

Author: Robson Kalata Nazareth¹ r.nazareth@ed.ac.uk
Advisor(s): Prashant Valluri¹
¹ University of Edinburgh

August 19, 2015

PPG-EM Seminars: season 2015
www.ppg-em.uerj.br

Keywords: Self-rewetting liquids; two-phase flow; thermocapillary migration.

1 Introduction

Thermocapillary migration is a phenomenon of bubble and drop motion driven by temperature-induced surface tension gradient. The variation of surface tension creates a tangential stress along the interface leading to interfacial flow from low to high surface tension regions, which drives fluid around on both sides of the interface. The motion of the neighboring fluid finally propels bubbles and drops in the opposite direction. This phenomenon is particularly important to understand instabilities in evaporative cooling of microelectronics due to the two-phase nature of the flow and the microscale characteristic of the system, where surface tension force become more relevant.

Since the pioneering work of Young et al. [3], that theoretically derived the terminal velocity of a bubble in a vertical temperature gradient, this subject has been extensively explored theoretically and experimentally for liquids where surface tension is a linearly decreasing function of temperature. For these liquids, bubbles migrate in direction to higher temperatures. However, little attention was given for self-rewetting liquids in this topic, i.e. binary mixtures, such as water/butanol, where surface tension is a parabolic function of temperature with a well defined minimum. These liquids have higher heat transfer coefficient than pure liquids, what make it attractive for phase-change based cooling applications. Shanahan and Sefiane [2] demonstrated that in self-rewetting liquids thermocapillary forces may drive bubbles away from high temperatures and against flow towards the surface tension minimum until reach an equilibrium position. At confinement conditions they observed that larger bubbles present sustained oscillations around the equilibrium position. The present study aim to complement this work by means of direct numerical simulations (DNS) in order to increase the comprehension of thermocapillary migration in self-rewetting fluids.

In this work, we consider an axisymmetric gas bubble of initial radius R traveling against flow in an axisymmetric horizontal channel of length L and diameter H , until reach the equilibrium position. Self-rewetting

liquid flow inside the channel with a fully developed Poiseuille velocity profile, and the channel wall is subjected to a temperature gradient, $\Gamma = (T_{hot} - T_{cold})/L$. The gas bubble is introduced at the downstream side of the channel (high temperatures) with zero initial velocity. We assume a thermodynamically saturated environment, with no phase change, and a negligibly small effect of gravity due to the microscale in consideration.

2 Model

The two-phase system is modeled with Gerris [1] using the Volume-of-Fluid method. The two fluids considered are incompressible, Newtonian and immiscible. The dimensionless governing equations for mass, momentum and energy conservation can be respectively written as:

$$\nabla \cdot \mathbf{u} = 0 \quad (1)$$

$$\rho \left[\frac{\partial \mathbf{u}}{\partial t} + \mathbf{u} \cdot \nabla \mathbf{u} \right] = -\nabla p + \frac{1}{Re} \nabla \cdot (\mu (\nabla \mathbf{u} + \nabla \mathbf{u}^T)) + \frac{1}{We} \mathbf{f}_{st} \quad (2)$$

$$\frac{\partial T}{\partial t} + \mathbf{u} \cdot \nabla T = \frac{1}{RePr} \nabla \cdot (\alpha \nabla T) \quad (3)$$

where \mathbf{u} , p and T are the velocity, pressure and temperature fields, and ρ , μ and α are the density, viscosity and thermal diffusivity, respectively. Time is denoted by t , and \mathbf{f}_{st} is the volumetric surface tension force. The dimensionless parameters are the Reynolds, Weber and Prandtl numbers given by $Re \equiv \rho_L V R / \mu_L$, $We \equiv \rho_L V^2 R / \sigma_0$ and $Pr \equiv \mu_L / (\rho_L \alpha_L)$, respectively, where V is the characteristic velocity and σ_0 is the reference surface tension coefficient.

The two phases are modeled using a “homogeneous” approach where both fluids obey the same set of governing equations and are represented by a single fluid with different properties locally identified by a volume fraction field c that can take 1 in the liquid phase, 0 in the gas phase and between 0 and 1 at the interface. In that sense, the single fluid volume averaged density, viscosity and thermal diffusivity read as $\rho = c + (1 - c)\rho_r$, $\mu = c + (1 - c)\mu_r$ and $\alpha = c + (1 - c)\alpha_r$, respectively, where $\rho_r = \rho_G / \rho_L$, $\mu_r = \mu_G / \mu_L$ and $\alpha_r = \alpha_G / \alpha_L$ are the density, viscosity and thermal diffusivity ratios and the subscript L stands for liquid and G for gas. The volume fraction field evolves in time across the domain

by the conservation equation,

$$\frac{\partial c}{\partial t} + \mathbf{u} \cdot \nabla c = 0 \quad (4)$$

The volumetric surface tension force in eq. (1) is denoted by $\mathbf{f}_{st} = (\sigma \kappa \mathbf{n} + \nabla_s \sigma) \delta_s$, where the first term is the normal component given by Laplace's formula and the second term is the tangent component given by surface tension gradient. The interface normal vector \mathbf{n} and the curvature κ are represented by, $\mathbf{n} = \nabla c / |\nabla c|$ and $\kappa = -(\nabla_s \cdot \mathbf{n})$. The gradient operator tangent to the interface is given by, $\nabla_s = \nabla - \mathbf{n}(\mathbf{n} \cdot \nabla)$ and the surface tension coefficient is represented by, $\sigma = 1 - \beta_1 T + \beta_2 T^2$, in order to model the self-rewetting fluid behaviour.

3 Results and Discussion

We analyse the effect of the thermal diffusion controlled by the Prandtl number, on the bubble thermocapillary motion. The base set of parameters derived from [2] is: $Re = 4.37$, $We = 4.22 \times 10^{-4}$, $\rho_r = 0.001$, $\mu_r = 0.01$, $\alpha_r = 0.04$, $\beta_1 = 0.3$, $\beta_2 = 0.15$, $\Gamma = 0.1$, $L = 80$, $H = 4$, $R = 1$, $U = 1$. In Fig. 1 we can see the initial conditions, where the initial bubble position is at $z_i = 70$, and the reference position for the temperature corresponding to the surface tension minimum, T_m , was chose as the location where its isothermal line (black line in Fig. 1) cross the center of the channel, at $z_m = 40$.

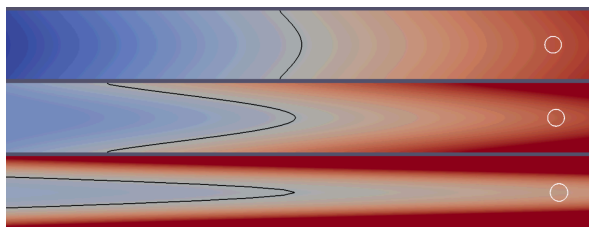


Figure 1: Initial conditions for $Pr = 0.1$ (top), $Pr = 1.0$ (middle) and $Pr = 6.1$ (bottom). The black line is the isothermal line for T_m , the white line is the bubble interface and the temperature contours is shown in colour.

In Fig. 2 we show the temporal evolution of the bubble center of mass during the counter-current thermocapillary motion in a channel with flow in the positive direction of z -axis. The bubble reach the equilibrium position through a damped oscillation motion and doesn't present sustained oscillations.

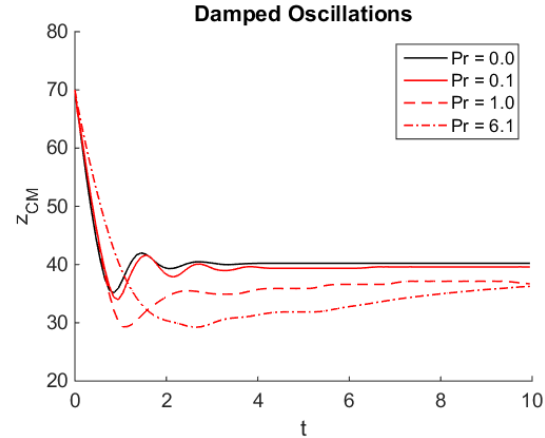


Figure 2: Temporal evolution of the bubble center of mass, z_{CM} , for different Prandtl numbers.

As we increased the Prandtl number towards realistic values ($Pr \approx 6.1$), we observed two effects of the thermal diffusion on bubble's motion: first, it delays the thermocapillary effect allowing higher amplitude oscillations; second, it weakness the thermocapillary effect, resulting in lower velocities for higher Prandtl numbers, as can be seen in Fig. 2. The first effect can be interpreted as a result of the decrease in thermal diffusion retarding the change of temperature at the bubble interface. The second effect can be explained by means of the temperature gradient vector field (perpendicular to the isothermal lines) that diverges from the z -direction as we increase the Prandtl number, and consequently decrease the net thermocapillary force in the direction parallel to bubble motion.

4 Future Work

The model will be extended to 3D to study confinement effects and avoid strong deviation of the temperature gradient vector field from the direction parallel to bubble motion, in order to capture the sustained oscillations.

References

- [1] S. Popinet. An accurate adaptive solver for surface-tension-driven interfacial flows. *J. of Comp. Physics*, 228:5838–5866, 2009.
- [2] M. E. R. Shanahan and K. Sefiane. Recalcitrant bubbles. *Nature Scientific Reports*, 4, 2014.
- [3] N. O. Young, J. S. Goldstein, and M. J. Block. The motion of bubbles in a vertical temperature gradient. *J. Fluid Mech.*, 6:350–356, 1959.



DEVELOPMENT OF A SAXS EQUIPMENT FOR NANOMATERIALS CHARACTERIZATION

Author: Rauni Coelho¹ *rauni.coelho@gmail.com*
Advisor(s): José Brant¹

¹ State University of Rio de Janeiro

September 16, 2015

PPG-EM Seminars: season 2015
www.ppg-em.uerj.br

Keywords: Small Angle X-Ray Scattering; X-ray Optics; collimators; X-ray bidimensional gas detector.

Abstract. With the increase use of nanomaterials increasingly seeking the creation of techniques and equipment to determine properties of interest in the nanometer scale. Thus, the technical SAXS (Small Angle X-Ray Scattering) allow the analysis of nanomaterials and determine various parameters such as particle size, density and morphology of nanoparticles. Normally, X-rays pass through the sample (the transmission mode) and each particle interacts with the X-ray emitting a signal which is detected and analyzed. As in all other areas of research, there are major challenges to the development of instrumentation for the application of this technique. The challenges of this research are the optical part of the project, from the platform of conventional X-ray diffraction equipment. The X-ray beam must have the smallest possible attenuation and this condition is obtained with the evacuation of all traveled optical path which includes the chamber where the sample is placed and the X-ray bidimensional gas detector.

1 Introduction

The devices that are used in the characterization of materials played an important role in the research of new materials. But many of them become obsolete when it comes to the study of nanomaterials. The SAXS equipment is a powerful tool in development and research at the nano scale, allowing the precise details of the structure of materials, defining the arrangements, shapes and the density of the crystalline structure. The progress made in the study and development of nanomaterials, emerged in parallel and as a result of these advances, the need to employ SAXS techniques to improve understanding of the different properties that these materials present in relation to the microscopic properties. Due to the cost fac-

tor, the instrumentation of this nature are extremely scarce in developing countries, as they are marketed with high values, in many cases prevents the acquisition of this equipment even by major educational institutions and research. Thus, from conventional X-ray diffraction equipment, instrumentation will enable the implementation of SAXS technique is developed, where the entire optical path traveled by the X-ray beams to reach the two-dimensional detector gas will be evacuated. Thus, from conventional X-ray diffraction equipment, instrumentation is developed which allow the application of the SAXS technique in which the entire optical path traveled by the X-ray beams to reach the bidimensional detector gas will be evacuated. The whole course of the X-ray beam, including the sample port should be free of particles that can reduce its intensity. The collimation of the flux of X-ray beams will also be developed.

2 Design and instrumentation

The base equipment, disposed for the preparation of this work is Siefert HGZ-4, which will go through two stages of reconstruction. In the first stage, this was done in partnership between the UERJ (Universidade Estadual do Rio de Janeiro) and the CBPF (Centro Brasileiro de Pesquisas Físicas), restructured and reshaped all the electronics and control system part as: replacement of stepper motor system, the encoder and the clutch system and the goniometer axis. The second stage is the part where this work is inserted, foresees the development of the SAXS optics, construction of the collimation system X-ray beam, the design and placement of the bidimensional detector. In the design of components that will compose the optical parts of the equipment are the gas detectors, developed and manufactured by CBPF,

which dominates this technology.

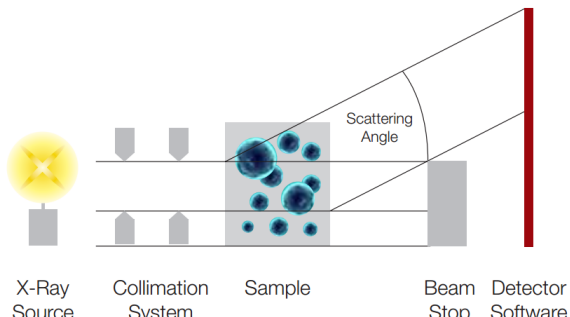


Figure 1: Schematic composed of (left to right): X-ray source, collimator, sample, scattering angle, beam stop and detector [1].

3 Results and discussion

This project because it is multiple steps and different areas of expertise, became a challenge that gradually has been overcome, since all the electronics and control system were completely reconstructed and finalized, getting ready to design phase and instrumentation that are underway and which will be

developed using national technology in the development of equipment that allows the use of SAXS techniques.

4 Conclusion

This design will contribute in the development of extreme importance equipment in the development and research of new materials and can be subjected to a patent, as the technology employed in gas detectors developed in CBPF holds an international patent and configuration of any instrumentation will compose this equipment, establishes a new application of this technology.

References

- [1] Heimo Schnablegger and Yashveer Singh. *The SAXS Guide: getting acquainted with the principles*. Anton Paar GmbH, 2013.

Acknowledgement

The authors thank CAPES for the financial support and CBPF, for their support and partnership.



COMPARATIVE ANALYSIS BETWEEN DIFFERENT TECHNIQUES FOR POROSITY MEASUREMENT APPLIED TO HIGH HARDNESS ADVANCED CERAMICS

Author: Vinicio Coelho¹ *viniciarj@gmail.com*
Advisor(s): Marilia Diniz¹

¹ State University of Rio de Janeiro

September 16, 2015

PPG-EM Seminars: season 2015
www.ppg-em.uerj.br

Keywords: Silicon Carbide, Porosity, Digital Image Processing, Archimedes Method.

1 Introduction

The search for high mechanical performance materials aroused great interest in the research and development of advanced ceramics such as silicon carbide (SiC). However, the porosity is still seen as a performance limiting factor of these. This work aims to quantify the porosity through analysis and digital imaging (DIP) obtained by optical microscopy with control of grinding and polishing parameters along various depths of advanced ceramic, followed by stacking these images through a 3D module to analyze the three-dimensional behavior of the pores. The methodology will be compared to the Archimedes method and computed tomography. The present results show that the DIP technique for the type and distribution of the pores existing been successful to a hard material characterization.

Silicon carbide (SiC) is highlight of ceramic class. This material has excellent mechanical properties at low and high temperatures, high wear resistance, high thermal stability and corrosion resistance. The unique characteristics of silicon carbide allow it to be used in various structural applications [1].

Some problems still limit the scope of silicon carbide, and other ceramic in general. The high cost of the manufacturing process, the difficulty of sintering and the control of porosity, together with the difficulty of more complex geometries. There are effective techniques for evaluation and quantification of the existing porosity in advanced ceramics, such as computed tomography, however, these techniques require high equipment and handling costs, which led to the search for alternatives that provide equally safe and less costly results, as quantitative stereology using the Digital Image Processing (DIP).

2 Methodology

Until now we used three samples 10x10x11mm provided by ESK manufacturer, Ekasic F group [1]. These samples were submitted to Archimedes procedure for density measurements, according to the NBR 6220 ABNT

[1]. They were embedded, ground and polished in nine layers (100, 200, 500, 1000, 2000, 3000, 4000, 5000 and 6000 μm) for obtaining optical microscopy images throughout the material. Following collection were 108 images of the surfaces of samples with an optical microscope (MO) Olympus BX60M, 36 for each sample (04 in each of the nine sections) in different regions of the surface. All were collected under 100x magnification.

The digital image processing was carried out through AxionVision software [1]. All images were processed individually and involved steps of preprocessing, segmentation and feature extraction. There was no need to eliminate "noise" and lighting correction for generating bimodal histograms for images.

3 Results and Discussion

Being commercial samples, the manufacturer claims that the degree of porosity of the material is less than 2.0% of its volume and its density is $3.15\text{g}/\text{cm}^3$. Figure 1 illustrates an image obtained by MO 100x magnification with a depth of 100 micrometres. The result after the segmentation step for extracting attributes and quantifying the number of pores present in the material is shown in Figure 2. In turn, Figure 3 is an image optical microscope with a magnification of 500x at a depth of 200 micrometres. The result of their digital processing is shown in Figure 4. Table 1 shows the silicon carbide densities obtained by the Archimedes method. Comparing the density obtained by this method with the theoretical value in this literature, a comparison is made where the difference between the values is the number of pores present in the material. Table 2, in turn, shows the porosity values obtained using the DIP

Porosity of sample 01 (%)	0.622
Porosity of sample 02 (%)	0.606
Porosity of sample 03 (%)	0.579
Average porosity of the material (%)	0.579

Table 1: Average porosities of three samples and SiC as a whole.

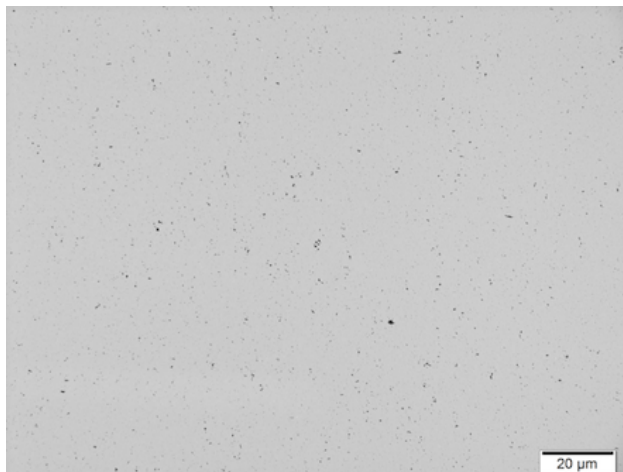


Figure 1: Optical microscopy image of SiC sample with 100x magnification after sanding and polishing at a depth of $100\mu\text{m}$.

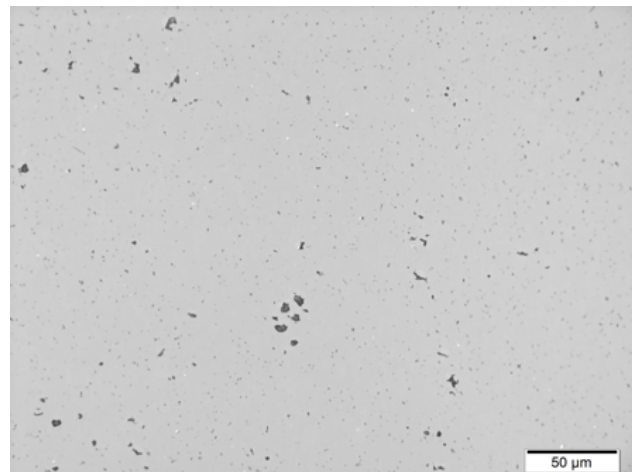


Figure 3: Optical microscopy image of SiC sample with 500x magnification after sanding and polishing at a depth of $200\mu\text{m}$.



Figure 2: Same image in Figure 1, but after digital processing to identify and quantify the presence of pores.



Figure 4: Same image in Figure 3, but after digital processing to identify and quantify the presence of pores.

Bulk density (g/cm^3)	Relative Density	Relative Density (%)
3.09	0.98	98.09
3.15	1.00	100.00
3.16	1.00	100.00
3.17	1.00	100.00
Average Porosity (%)	0.48	0.82

Table 2: Measurements of relative and apparent densities of SiC by Archimedes method.

4 Conclusions

It was found that the percentage porosities found for the methods of Archimedes and PDI showed a great similarity ($0.48\%\pm 0.82$ by Archimedes and $0.6\%\pm 0.018$ per PDI) and did not exceed the 2.0 limit % stipulated by the manufacturer for ESK lot Ekasic F SiCa detailed procedure has been prepared that will serve as guide for future research. The Digital Image Processing had credibility stated for the tested samples, proved to be a suitable method which is based on quantitative metallographic procedures.

5 Acknowledgments

At FAPERJ, for the financial support; the UFRJ Advanced Ceramics Laboratory, and the Microscopy Laboratory of CEFET / RJ.

References

- [1] V.S. Coelho. Porosity measure digital sic processing through images. Master's thesis, State University of Rio de Janeiro, UERJ, 2015.



MODELING AND SIMULATION OF POLYDISPERSED MULTIPHASE FLOW

Author: Prof. D.Sc Fabio Pereira dos Santos¹ (fabio.santos@uerj.br)

Author: Prof. D.Sc Paulo Laranjeira da Cunha Lage²

¹ Rio de Janeiro State University, Mechanical Engineering Department;

² Federal University of Rio de Janeiro, Chemical Engineering Department (COPPE/UFRJ);

PPG-EM Seminars: season 2015

www.ppg-em.uerj.br

Keywords: Population balance, Multiphase flow, CFD, polydispersed flow the particle-particle and particle-fluid interactions.

1 Introduction

Polydispersed multiphase flows are present in several natural and industrial processes, and involve a series of physical phenomena, such as: transfer of mass, momentum and energy. In bubble column chemical that are used in the biochemical and petrochemical industries, reactor efficiency significantly depends on interfacial area of the bubbles and the resident time. Therefore, the particle size distribution (PSD) is a parameter whose behavior is important to control this process. In material science, the precipitation reaction is another good example of polydispersed multiphase flow. In this case, reaction happens in a liquid phase with some chemical substances that react to form a solid with some specific features. The final market value of the crystallized product is strongly dependent on its PSD. For these reasons, modeling and simulation of polydispersed multiphase flow is critically important. In this work, we describe a computational framework to simulate polydispersed multiphase flows based on population balance equations (PBE), and we also discuss which numerical methods is suitable to couple the solution of PBE with CFD simulations.

2 Mathematical Model

Three main approaches can be used to model polydispersed multiphase flows: the fully-resolved, the Lagrangian point-particle and the Eulerian-Eulerian model [6]. In the Eulerian-Eulerian (E-E) models, the phase equations are derived for their mean variables, that are closed by constitutive relations obtained from empirical data [3]. This average procedure yields equations with a reasonable computational cost and accuracy for complex problem in large scale. Nonetheless, this model by itself can not capture particle-particle interactions, such as aggregation and breakage phenomena. In order to overcome this limitation a mesoscale framework called population balance model (PBM), which is the conservation equation for the number of particles represented by a number density function (NDF) [6], can be combined with a multi-fluid flow formulation [5] to predict

2.1 Eulerian Multiphase Model

The Eulerian-Eulerian multiphase equations are derived by the averaging process in conservation equations. The result of this averaging procedure yields the mass conservation equation for the each phase below [6]:

$$\frac{\partial(r_\alpha \rho_\alpha)}{\partial t} + \nabla \cdot (r_\alpha \rho_\alpha \mathbf{u}_\alpha) = \Gamma_\alpha, \quad (1)$$

where ρ_α is the density, Γ_α is a mass source term and \mathbf{u}_α is the velocity of the phase α , where $\alpha = 0 \dots N$. In this equation, the volume fraction, r_α , appears as the probability of a phase α exists in the space and time regarding all possible realizations.

Extending the same procedure to momentum conservation equations for the α phase, the following averaged equation is obtained:

$$\begin{aligned} \frac{\partial(r_\alpha \rho_\alpha \mathbf{u}_\alpha)}{\partial t} + \nabla \cdot (r_\alpha \rho_\alpha \mathbf{u}_\alpha \mathbf{u}_\alpha) &= -r_\alpha \nabla p_\alpha + \quad (2) \\ \nabla \cdot (r_\alpha \rho_\alpha \tau_\alpha^{\text{eff}}) + r_\alpha \rho_\alpha \mathbf{g} + \Gamma_\alpha \mathbf{u}_\alpha + \sum_{\substack{\beta=0 \\ \beta \neq \alpha}}^N \mathbf{M}_{\alpha,\beta}, \end{aligned}$$

where τ_α^{eff} is the effective stress tensor, which has the effects of viscous stress tensor and turbulent stress tensor. $\mathbf{M}_{\alpha,\beta}$ represents the interfacial momentum exchanged between the phases α and β . It is usually broken into drag force, lift force, virtual mass force, average interfacial pressure and shear stress at the interface.

2.2 Population Balance Modeling

The PB-CFD coupling has proved to be well-suited to predict polydispersed multiphase flows [5, 1, 2]. In this work, the following inhomogeneous monovariate PBE with an additive internal variable, x , is used:

$$\frac{\partial f(x, \mathbf{z}, t)}{\partial t} + \nabla_{\mathbf{z}} \cdot [\mathbf{u}_d f(x, \mathbf{z}, t)] = S(x, \mathbf{z}, t) + R(x, \mathbf{z}, t), \quad (3)$$

where $S(x, \mathbf{z}, t)$ is an additional source term, x is an internal variable for diameter, \mathbf{z} is the physical space coordinates and $R(x, \mathbf{z}, t)$ is given by the equation below:

$$R(x, \mathbf{z}, t) = \mathcal{L}_b f(x, \mathbf{z}, t) + \mathcal{L}_a f(x, \mathbf{z}, t). \quad (4)$$

The \mathcal{L}_b and \mathcal{L}_a are, respectively, the breakage and aggregation operators.

3 PB-CFD coupling with DQBMMs

The DQBMM-PB-CFD coupling is very similar to QBMM-PB-CFD coupling [5]. Again, each Gauss-Christoffel quadrature node is assigned to one dispersed phase α , and when their abscissas are the particle volume, the weighted abscissa, ζ_α , is equivalent to its volume fraction in an incompressible flow. Furthermore, if the particles are considered spherical, the particle volume can be converted into the particle diameter, and therefore, used to calculate the interfacial force between the continuous and dispersed phases in each CFD cell.

4 Results and Discussions

In order to verify the PB-CFD coupling with DQBMMs, we applied this approach with some tool models. The DQBMM-PB-CFD code verification is carried out in a two dimensional Backward Facing Step (BFS) geometry, due to its simplicity and well-defined recirculation zones, where the effects of particle interaction are predominant. DQBMM-PB-CFD code, implemented in OpenFOAM, is simulated with unrealistic problems with breakage and aggregation kernels described in the following.

4.1 Simultaneous breakage and aggregation cases

The simultaneous breakage and aggregation problem proposed by McCoy and Madras [4] is simulated to compare the results of DQMoM, DuQMoGeM and Direct DuQMoGeM using 4 moments. Regarding to the simulations result, from Figure 1, one can see that, the recirculation zones on the BFS is evident right after the step. In these regions the residence time of dispersed phase is longer and the aggregation and breakage effects are higher.

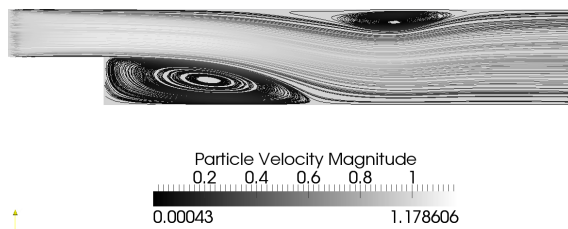


Figure 1: Velocity magnitude of the dispersed phase for breakage case with 6000 nodes mesh and tolerance of 1×10^{-6} at 0.3 seconds.

From Figure 2, we can observe that in recirculation zone the emulsion starts to break as was expected. This result was represented by Silva and Lage [5] using traditional DQMoM.

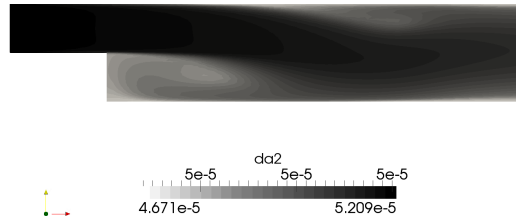


Figure 2: Diameter of dispersed phase with 6000 nodes mesh and tolerance of 1×10^{-6} at 0.3 seconds.

5 Conclusions

In this work, a polydispersed multiphase flow model using dual quadrature-based moments methods were implemented in OpenFOAM and parallelized on GPUs. In order to verify the code, the DQBMM-PB-CFD coupling were applied to an oil-water emulsion and their results were compared to the same code using DQMoM. The results were similar. However, we can consider that the dual quadrature-based moments methods are more accurate, once they can control the quadrature error present in DQMoM.

6 Acknowledgments

Paulo L. C. Lage and Fabio P. Santos acknowledge the financial support of CNPq, grants nos. 302963/2011-1, 476268/2009-5 and 140794/2010-7. We also would like to thank Prof. Gustavo R. dos Anjos.

References

- [1] A. Buffo, M. Vanni, D.L. Marchisio, and R.O. Fox. Multivariate quadrature-based moments methods for turbulent polydisperse gas–liquid systems. *International Journal of Multiphase Flow*, 50(0):41 – 57, 2013.
- [2] F. Doisneau, F. Laurent, A. Murrone, J. Dupays, and M. Massot. Eulerian multi-fluid models for the simulation of dynamics and coalescence of particles in solid propellant combustion. *Journal of Computational Physics*, 234(0):230 – 262, 2013.
- [3] M. Ishii and T. Hibiki. *Thermo-fluid dynamics of two-phase flow*. Birkhäuser, 2006.
- [4] Benjamin J. McCoy and Giridhar Madras. Analytical solution for a population balance equation with aggregation and fragmentation. *Chemical Engineering Science*, 58(13):3049 – 3051, 2003.
- [5] L.F.L.R. Silva and P.L.C. Lage. Development and implementation of a polydispersed multiphase flow model in OpenFOAM. *Computers & Chemical Engineering*, 35(12):2653 – 2666, 2011.
- [6] Guan Heng Yeoh and Jiyuan Tu. *Computational Techniques for Multiphase Flows*. Butterworth-Heinemann, Oxford, 2010.